

Deep low-frequency radio observations of Abell 2256

II. The ultra-steep spectrum radio halo[★]

K. Rajpurohit^{1,2,3} , E. Osinga⁴, M. Brienza^{5,1,2}, A. Botteon^{1,2,4}, G. Brunetti², W. R. Forman⁶, C. J. Riseley^{1,2,7}, F. Vazza^{1,2,8}, A. Bonafede^{1,2}, R. J. van Weeren⁴, M. Brüggen⁸, S. Rajpurohit⁹, A. Drabent³, D. Dallacasa¹, M. Rossetti¹⁰, A. S. Rajpurohit¹¹, M. Hoeft³, E. Bonnassieux¹², R. Cassano², and G. K. Miley⁴

¹ Dipartimento di Fisica e Astronomia, Università di Bologna, via P. Gobetti 93/2, 40129 Bologna, Italy
e-mail: kamlesh.rajpurohit@unibo.it

² INAF – Istituto di Radio Astronomia, Via Gobetti 101, 40129 Bologna, Italy

³ Thüringer Landessternwarte (TLS), Sternwarte 5, 07778 Tautenburg, Germany

⁴ Leiden Observatory, Leiden University, PO Box 9513, 2300 RA Leiden, The Netherlands

⁵ INAF – Osservatorio di Astrofisica e Scienza dello Spazio di Bologna, via Gobetti 93/3, 40129 Bologna, Italy

⁶ Harvard-Smithsonian Center for Astrophysics, 60 Garden Street, Cambridge, MA 02138, USA

⁷ CSIRO Space & Astronomy, PO Box 1130, Bentley, WA 6102, Australia

⁸ Hamburger Sternwarte, Universität Hamburg, Gojenbergsweg 112, 21029 Hamburg, Germany

⁹ Molecular Foundry, Lawrence Berkeley National Laboratory, Berkeley, CA 94720, USA

¹⁰ INAF – IASF Milano, via A. Corti 12, 20133 Milano, Italy

¹¹ Astronomy & Astrophysics Division, Physical Research Laboratory, Ahmedabad 380009, India

¹² Lehrstuhl für Astronomie, Universität Würzburg, Campus Hubland Nord, Emil-Fischer-Strasse 31, 97074 Würzburg, Germany

Received 8 September 2022 / Accepted 19 October 2022

ABSTRACT

We present the first detailed analysis of the radio halo in the merging galaxy cluster Abell 2256 using the LOw Frequency ARray, the upgraded Giant Metrewave Radio Telescope, and the *Karl G. Jansky* Very Large Array. Radio observations (120 MHz–2 GHz) combined with archival *Chandra* and *XMM-Newton* X-ray data allowed us to study the central radio halo emission with unprecedented detail. The integrated radio emission from the entire halo is characterized by an ultra-steep spectrum, which can be described by a power law with $\alpha_{144\text{MHz}}^{1.5\text{GHz}} = -1.63 \pm 0.03$ and radial steepening in the outer regions. The halo is significantly underluminous according to the current scaling relations between radio power and mass at 1.4 GHz, not at 150 MHz; ultra-steep spectrum halos are predicted to be statistically underluminous. Despite the complex structure of this system, the halo morphology is remarkably similar to that of the X-ray emission. The radio surface brightness distribution across the halo is strongly correlated with the X-ray brightness of the intracluster medium. The derived correlations show sublinear slopes and distinct structures: the core is $I_R \propto I_X^{1.51}$, the outermost region $I_R \propto I_X^{0.41}$, and we find radio morphological connections with X-ray discontinuities. We also find a strong anticorrelation between the radio spectral index and the X-ray surface brightness, implying radial steepening. We suggest that the halo core is either related to old plasma from previous active galactic nuclei activity, being advected, compressed, and reaccelerated by mechanisms activated by the cold front or less turbulent with strong magnetic field in the core. The change in the radio versus X-ray correlation slopes in the outer regions of the halo could be due to a radial decline of the magnetic field, the increase in the number density of seed particles, or increasing turbulence. Our findings suggest that the emitting volume is not homogenous according to turbulent reacceleration models.

Key words. galaxies: clusters: individual: Abell 2256 – galaxies: clusters: intracluster medium – acceleration of particles – radiation mechanisms: non-thermal – large-scale structure of Universe – turbulence

1. Introduction

Galaxy clusters undergoing mergers often show megaparsec-scale radio relics and radio halos (see Brunetti & Jones 2014; van Weeren et al. 2019, for a recent review). These halos and relics provide direct evidence for the presence of magnetic fields and relativistic particles which are mixed with the thermal intracluster medium (ICM). The radio spectra¹ of such sources are steep ($\alpha \leq -1.0$). The origin of the radiating relativistic particles that produce halos and relics has not been fully understood.

[★] Reduced images are also available at the CDS via anonymous ftp to cdsarc.cds.unistra.fr (130.79.128.5) or via <https://cdsarc.cds.unistra.fr/viz-bin/cat/J/A+A/669/A1>

¹ $S_\nu \propto \nu^\alpha$, with spectral index α .

Radio halos are found at the centers of galaxy clusters where the radio emission typically follows the thermal X-ray surface brightness. One of the leading models involves the reacceleration of cosmic-ray electrons (CRE) by the interaction with turbulence injected into the ICM in connection with cluster mergers (Brunetti et al. 2001; Petrosian 2001; Brunetti & Lazarian 2007, 2016; Beresnyak et al. 2013; Miniati 2015). This model can explain the connection with cluster dynamics (Cassano et al. 2010, 2013; Cuciti et al. 2021) and the complex spectral properties observed in the population of radio halos, including the existence of ultra-steep spectrum ($\alpha \leq -1.5$) halos (Brunetti et al. 2008; Dallacasa et al. 2009; Wilber et al. 2018; Rajpurohit et al. 2021a; Bruno et al. 2021; Di Gennaro et al. 2021; Duchesne et al. 2021) and the presence of large-scale fluctuations in the spectral

index distribution (Botteon et al. 2020a; Rajpurohit et al. 2021a,b; Bonafede et al. 2022).

Gamma-ray observations for clusters hosting radio halos suggest that secondary emission from p-p collisions between relativistic and thermal protons in the ICM are subdominant (Brunetti et al. 2012; Ackermann et al. 2014, 2016), yet turbulent reacceleration of these secondary particles is still consistent with radio and gamma-ray observations (Brunetti et al. 2017; Pinzke et al. 2017; Adam et al. 2021). In recent years, the picture has become more complicated as some clusters hosting mini halos, believed to be associated with sloshing motions of the ICM, have been found to also contain a large-scale steep spectrum radio component with properties similar to radio halos (e.g., Biava et al. 2021, Riseley et al. 2022b).

In this paper, we focus on the radio halo in the galaxy cluster Abell 2256. A detailed analysis of the large filamentary relic is presented in Rajpurohit et al. (2022a; hereafter Paper I). Due to strong emission at radio and X-ray wavelengths, low redshift, the presence of several X-ray surface brightness discontinuities (cold fronts and shock fronts), and its large angular extent, the Abell 2256 is excellently suited to test currently proposed acceleration models for radio halo formation. High-resolution radio observations over a wide frequency range are essential to improve our understanding of the particle acceleration in radio halos. Since halos are low surface brightness sources, only a few systems, including Abell 2256, allow for detailed investigations with current instruments. We use data from the LOw-Frequency ARray (LOFAR), upgraded Giant Metrewave Radio Telescope (uGMRT), and the *Karl G. Jansky* Very Large Array (VLA). The uGMRT observations are originally published in Paper I and the LOFAR high band antenna (HBA) in Osinga et al. (in prep.). These sensitive wideband observations allowed us to study the low-surface brightness halo emission at a higher resolution than has been done previously. To compare the radio and X-ray properties, and the connection between the thermal and nonthermal plasma of the ICM, we used archival *Chandra* and *XMM-Newton* observations.

The layout of this paper is as follows: In Sect. 3, we present an overview of the observations and data reduction. The new radio images are presented in Sect. 4. The results obtained with radio and X-ray analysis are described in Sect. 5, followed by a summary in Sect. 6.

Throughout this paper, we adopt a flat Λ CDM cosmology with $H_0 = 69.6 \text{ km s}^{-1} \text{ Mpc}^{-1}$, $\Omega_m = 0.286$, and $\Omega_\Lambda = 0.714$. At the cluster's redshift, $1''$ corresponds to a physical scale of 1.13 kpc. All output images are in the J2000 coordinate system and are corrected for primary beam attenuation.

2. Abell 2256

Abell 2256 is a massive nearby cluster ($z = 0.058$) that exhibits strong emission at all wavelengths. In the radio domain (see Figs. 1 and 2), the cluster is characterized by complex diffuse emission on a large scale that consists of an extended steep spectrum radio halo at the center of the cluster, which is surrounded by a giant filamentary relic to the northwest and several complex radio sources (Bridle & Fomalont 1976; Bridle et al. 1979; Rottgering et al. 1994; Kim 1999; Clarke & Ensslin 2006; Brentjens 2008; van Weeren et al. 2009b, 2012; Owen et al. 2014; Rajpurohit et al. 2022a). The existence of a radio halo in Abell 2256 was first suggested by Bridle et al. (1979) using Westerbork Synthesis Radio Telescope at 610 MHz. The presence of halo emission was shown at both low- and high-frequency from 63 MHz to 1.4 GHz (Clarke & Ensslin 2006;

Brentjens 2008; Kale & Dwarakanath 2010; van Weeren et al. 2012; Owen et al. 2014). In fact, some of these studies reported the properties of the large relic, which was misinterpreted as halo emission. Therefore, detailed morphology, size, and characterization of the halo emission remained missing, mostly because of poor resolution, the lack of adequate sensitivity, and possible overlap between the halo, relic, and nearby radio galaxies.

The cluster has a total mass of about $M_{500} = (6.1 \pm 0.4) \times 10^{14} M_\odot$ (Planck Collaboration XI 2011; Markevitch & Vikhlinin 1997). The dynamical state of the cluster is complex, as suggested by both optical and X-ray observations. Optical studies of the galaxy distribution reveal that the cluster consists of three separate mass components (Berrington et al. 2002; Miller et al. 2003). These studies provide strong evidence that Abell 2256 is undergoing a merger event between a main cluster component, a major subcomponent, and a third infalling group (Fabricant et al. 1989; Berrington et al. 2002; Miller et al. 2003; Ge et al. 2020).

At X-ray wavelengths, the cluster is luminous ($L_{X,0.1-2.4 \text{ keV}} = 3.7 \times 10^{44} \text{ erg s}^{-1}$; Ebeling et al. 1998). The cluster is very rich in X-rays consisting of several substructures, (Fabricant et al. 1989; Briel et al. 1991; Briel & Henry 1994; Roettiger et al. 1995; Molendi et al. 2000; Sun et al. 2002; Ge et al. 2020; Breuer et al. 2020). *Chandra* and *XMM-Newton* studies provide evidence for several X-ray surface brightness discontinuities (Sun et al. 2002; Bourdin & Mazzotta 2008; Trasatti et al. 2015; Ge et al. 2020; Breuer et al. 2020).

3. Observations and data reduction

3.1. Radio observations: LOFAR, uGMRT, and VLA

We observed the cluster with the uGMRT in Band 4 (550–950 MHz), Band 3 (300–450 MHz), and LOFAR (120–168 MHz; Osinga et al., in prep.). We also used archival VLA observations. In Table 1, we summarize the observational details. For a detailed description of uGMRT, LOFAR, and VLA observations and the data reduction, we refer readers to Paper I. In summary, the wideband uGMRT data were processed using the Source Peeling and Atmospheric Modeling (SPAM; Intema et al. 2009), pipeline². The LOFAR HBA data reduction and calibration were performed with the LoTSS DR2 pipeline (Tasse et al. 2021) followed by the final “extraction+self-calibration” scheme (van Weeren et al. 2021). The VLA A, B, C, and D configurations data were calibrated in CASA (see Paper I).

The final deconvolution was performed in WSClean (Offringa et al. 2014) using multiscale and Briggs weighting with a robust parameter -0.5 . The output images presented in this work were corrected for primary beam attenuation. The uncertainty in the flux density measurements was estimated as:

$$\Delta S = \sqrt{(f \cdot S)^2 + N_{\text{beams}} (\sigma_{\text{rms}})^2}, \quad (1)$$

where f is an absolute flux density calibration uncertainty, S_ν is the flux density, σ_{rms} is RMS noise, and N_{beams} is the number of beams. We assume absolute flux density uncertainties of 10% for uGMRT Band 3 (Chandra et al. 2004) and LOFAR data (Shimwell et al. 2022), 5% for uGMRT Band 4 data, and 2.5% for VLA data (Perley & Butler 2013).

² <http://www.intema.nl/doku.php?id=huibintemaspampipeline>

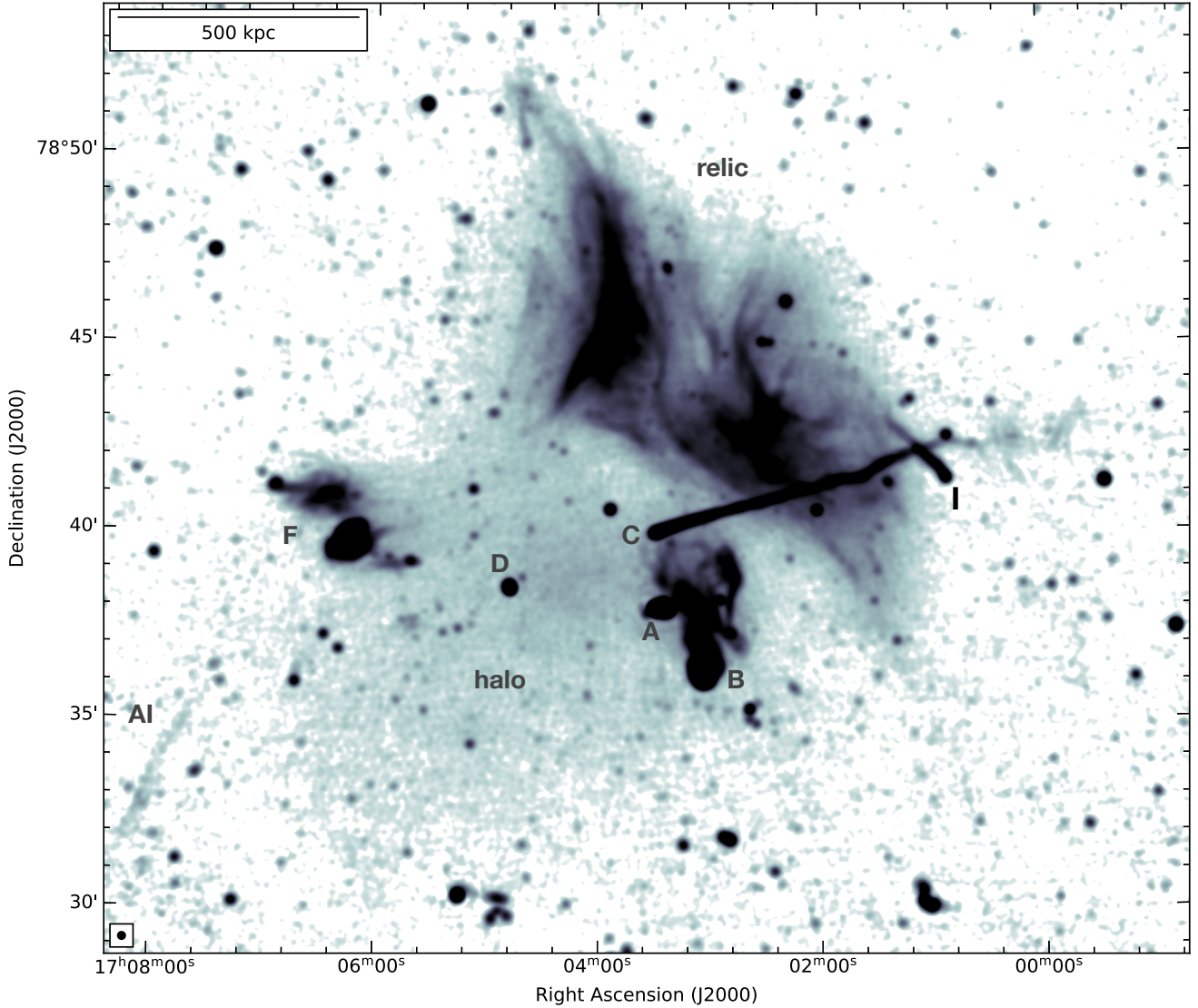


Fig. 1. uGMRT Band 4 (550–850 MHz) image of the galaxy cluster Abell 2256 with an angular resolution of $12''$, highlighting the spectacular central halo emission, the filamentary relic, and radio galaxies in the field. The beam size is indicated in the bottom left corner of each image. The image is created with Briggs weighting using $\text{robust} = -0.5$. The rms is $14 \mu\text{Jy beam}^{-1}$.

3.2. X-ray observations: *Chandra* and *XMM-Newton*

We reprocessed the four archival *Chandra* ACIS-I observations of Abell 2256 that are listed in Table 2 together with their individual net exposure time. We note that three other ACIS-S observations are present in the *Chandra* archive (ObsIDs: 965, 1521, 2419) but these were not considered in this work because of the smaller field of view of ACIS-S and shorter exposure times. Data were processed with CIAO v4.12 and *Chandra* CaLDB v4.9.0 using `chandra_repro` to produce new level=2 event files. Periods of observations affected by soft proton flares were removed with task `deflare` after inspecting the light curves extracted from the S2 chip in the 0.5–0.7 keV band. The five ObsIDs were combined with `merge_obs` to produce an exposure-corrected mosaic image of the cluster in the 0.5–2.0 keV band.

We combined the individual exposure-corrected point spread function (PSF) of each ObsID to produce a single PSF map with minimum size that was passed to the task `wavdetect` to detect point sources in the mosaiced image. Point sources were detected using wavelet radii of 1, 2, 4, 8, and 16 pixels that are removed by replacing the pixels inside the

point source regions with randomized values from surrounding regions.

We also produced an *XMM-Newton* mosaic image of Abell 2256 in the 0.5–2.0 keV band, obtained using 8 archival observations (for ObsIDs, see Table 2). Each single ObsID was processed using the *XMM-Newton* Scientific Analysis System (SAS v16.1.0) and the Extended Source Analysis Software (ESAS) data reduction scheme. After this count images, background images, and exposure maps of each observation were combined to produce background-subtracted and exposure-corrected image. This image covers a larger field of view than *Chandra* observations and was used to study the radio and X-ray correlations.

4. Results: Radio and X-ray morphology

4.1. Radio halo emission

The uGMRT 550–850 MHz image of the cluster Abell 2256 is shown in Fig. 1 at a resolution of $12''$. The image shows a large filamentary relic to the north and several peculiar radio galaxies,

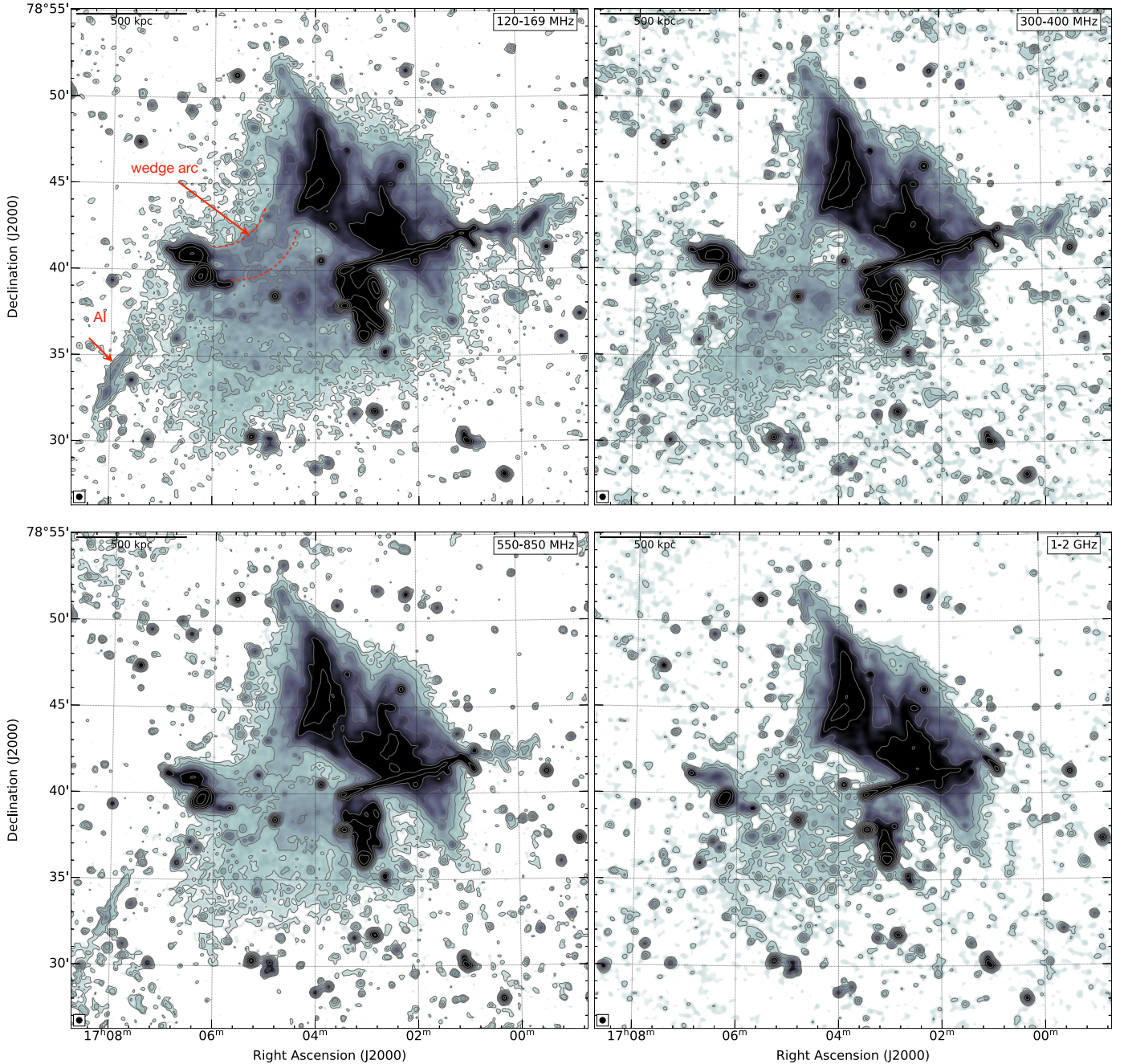


Fig. 2. Low resolution LOFAR 144 MHz (Osinga et al. in prep), uGMRT (300–950 MHz), and VLA *L*-band images of Abell 2256 in square root scale. All images are created at a common $20''$ resolution. The radio surface brightness unit is mJy beam^{-1} . The beam size is indicated in the bottom left corner of each image. Contour levels are drawn at $[1, 2, 4, 8, \dots] \times 3.0 \sigma_{\text{rms}}$, where $\sigma_{144 \text{ MHz, rms}} = 180 \mu\text{Jy beam}^{-1}$, $\sigma_{350 \text{ MHz, rms}} = 44 \mu\text{Jy beam}^{-1}$, $\sigma_{675 \text{ MHz, rms}} = 18 \mu\text{Jy beam}^{-1}$ and $\sigma_{1.5 \text{ GHz, rms}} = 10 \mu\text{Jy beam}^{-1}$. These images highlight the morphology of the halo emission with observing frequency and show that the halo is much more extended toward low frequencies. There are two other distinct features: an arc-shaped wedge to the east (show within red dotted curves) and source AI to the southwest.

see Paper I. The central region of the cluster is dominated by the large-scale low surface brightness halo emission, which is the primary focus of this paper, and radio galaxies A, B, and C. The detailed analysis of radio galaxies in the field will be presented in a subsequent paper.

In comparison to all the previously published total power continuum images, our detection of the halo is of higher significance and the morphology of the halo is more precisely characterized. As shown in Fig. 1, at 550–850 MHz, the large part of the halo is apparently elongated in the northwest and southeast

direction, that is along the merger direction. Brentjens (2008) reported the presence of filamentary substructures within the halo region. In contrast, none of our new images show filamentary substructures embedded within the halo region. The total extent of the halo emission is larger than previously reported at a similar frequency (Bridle & Fomalont 1976; Intema et al. 2009). In the published 610 MHz images, mainly the innermost part of the halo is detected, while the low surface brightness emission is not completely recovered very likely because of the poor uv-coverage at short baselines and low sensitivity. From our new

Table 1. Observational overview: uGMRT, LOFAR, and VLA observations.

	LOFAR HBA (**)	uGMRT Band 3	uGMRT Band 4	VLA <i>L</i> -band (‡)
Frequency range	120–169 MHz	300–500 MHz	550–950 MHz	1–2 GHz
Channel width	12.2 kHz	97 kHz	49 kHz	1 MHz
No of channels	64	4096	4096	64
On source time	16 h	10 h	8 h	24 h
LAS (*)	228′	32′	17′	16′

Notes. Full Stokes polarization information was recorded for the uGMRT Band 4, Band 4, and VLA *L*-band. For the VLA, the number of spectral windows are 16 each with 64 channels. (**)For data reduction of the LOFAR 144 MHz and uGMRT, VLA observations, we refer readers to Osinga et al. (in prep.) and Paper I, respectively. (‡)Archival VLA *L* band data. (*)Largest angular scale (LAS) that can be recovered by the mentioned observations.

Table 2. *Chandra* and *XMM-Newton* observations used in this work.

	ObsID	Net time (ks)	Observing date
<i>Chandra</i>	16129	44.5	August, 14 2014
	16514	44.5	August, 17 2014
	16515	43.2	September, 07 2014
	16516	44.5	September, 26 2014
<i>XMM-Newton</i>	0112500201	10.1, 8.6, 4.2	March, 20 2002
	0112950501	3.8, 3.1, 0.6	March, 20 2002
	0112950601	10.8, 11.8, 5.9	March, 28 2002
	0112950801	11.0, 5.4, 0.8	March, 30 2002
	0112950901	0.5, 0.5, 1.7	April, 23 2002
	0401610101	38.9, 35.3, 14.5	April, 19 2002
	0112951501	8.5, 8.9, 6.4	June, 02 2002
	0112951601	10.3, 10.8, 5.5	September, 22 2002

Notes. The net time for *XMM-Newton* refers to the net time for each detector (mos1,mos2,pn).

image, the exact largest linear size (LLS) of the halo is difficult to measure because of the presence of the relic and several other complex sources. But the LLS of the halo is at least ~ 750 kpc at 675 MHz. Additionally, we found about 48 unrelated compact sources ($>3\sigma_{\text{rms}}$) embedded in the halo region.

For morphological comparison, in Fig. 2 we show the moderate resolution ($20''$) LOFAR (120–169 MHz), Band 3 (300–400 MHz), Band 4 (550–850 MHz), and VLA (1–2 GHz) images. The shape of the radio halo is similar in these images. From Fig. 2, it is evident that the halo is more extended toward low frequencies. We emphasize that the radio observations presented in this paper are very deep and sensitive to low surface brightness emission. The halo appears to shrink at high frequencies due to the steepening in the outermost regions, as discussed in Sect. 5.1. This has been recently observed also in other giant halos, for example MACSJ0717.5+3745 and Abell 2744 (Rajpurohit et al. 2021a,b). The LLS size of halo at 144 MHz and 1.5 GHz is 900 kpc and 480 kpc, respectively. The entire halo covers an area of about 721 kpc \times 900 kpc, 560 kpc \times 750 kpc, and 490 kpc \times 480 kpc at 144 MHz, 675 MHz, and 1.5 GHz, respectively.

In 144 and 350 MHz images, the radio surface brightness is enhanced in the region between source D and source A. The dominant blob-like emission feature to the west of source D coincides with the cluster core; see Fig. 2. The radio surface brightness across the halo is fainter than the relic emission and sources F and B. In radio maps, in particular at 144 MHz, the southern edge of the halo follows a V-shaped morphology with the bottom of the V at the southeast.

A distinct morphological structure is an arc-shaped structure (labeled as wedge arc in Fig. 2) at the northeast of the cluster, first reported by Owen et al. (2014) at 1–2 GHz. No feature is detected in *Chandra* or *XMM-Newton* X-ray images at this location (Ge et al. 2020). The wedge arc is apparently connected to the large relic, the central halo emission, and the source F. On the basis of only the visual appearance, whether the connection between these features is real or just in projection is not obvious. We note that the wedge arc is very likely associated with the halo, as discussed later in Sect. 5.4, therefore in the remainder of the paper this region is considered as part of the halo emission.

There is a linear structure, labeled AI in Fig. 2, to the southeast of the cluster. It is located at a projected distance of about 1 Mpc from the cluster center and was previously detected by van Weeren et al. (2009a) and Intema et al. (2009). We do not find any optical counterpart for this source. At 350 MHz, the LAS of the source is $403''$ corresponding to a physical size of 455 kpc at the cluster redshift. We measure a flux density of 4.3 ± 0.2 mJy at 675 MHz. The source is not detected at 1–2 GHz and its overall spectrum is curved. We obtained a radio power of $P_{1.5\text{ GHz}} = 3.7 \times 10^{22}$ W Hz $^{-1}$ using the spectral index of -1.9 between 350 and 675 MHz.

4.2. X-ray emission

X-ray observations of Abell 2256 suggest a complex dynamical state. The cluster has two bright peaks in the X-ray surface brightness distribution corresponding to a primary cluster (main component) and a subcomponent (“mouth”) to the west, see Fig. 3 for labeling. The main component has a prominent peak (P1). This peak in the main cluster is also the center of the cluster (core), while the other peak is about 250 kpc to the west in the subcomponent. Optical observations also suggest a third poorer subcomponent to the north of the cluster which is infalling onto the main component from the northeast (Sun et al. 2002; Miller et al. 2003).

In Fig. 3, we compare the X-ray morphology of the cluster with that of radio emission at 675 MHz (top panel) and 144 MHz (bottom panel). The radio halo emission at 675 and 144 MHz largely follows the X-ray surface brightness distribution. In both radio and X-ray, the main component is elongated along the southeast-northwest direction. Radio emission from the halo extends over the entire region of the detected X-ray emission.

From Figs. 3 and 4, it is evident that the innermost bright halo core (P1) coincides with the bright X-ray emission in the main component. Within P1, there are two X-ray peaks but none of them coincide with the halo peak in the radio. This suggests that the main component core does not coincide with the peak

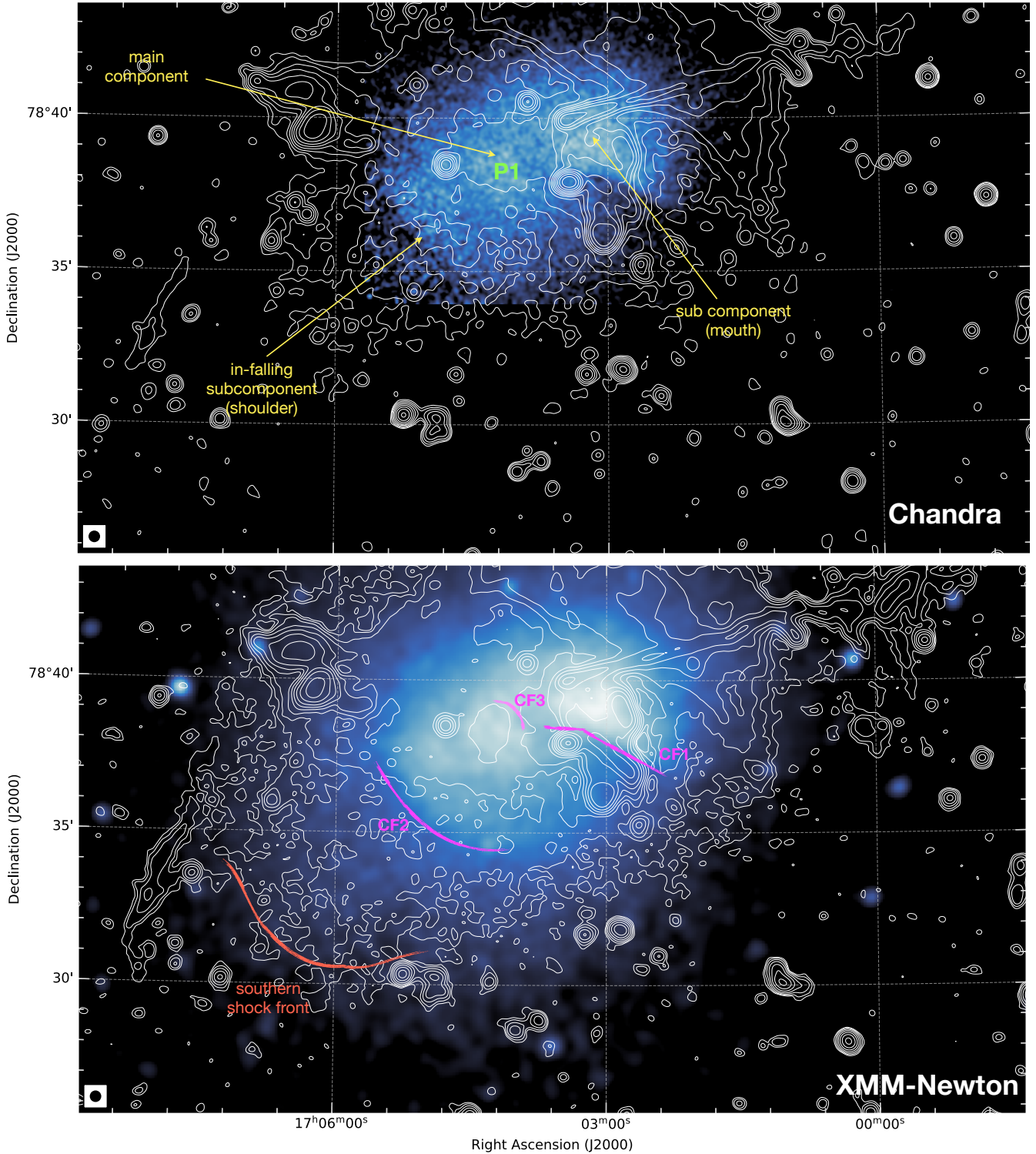


Fig. 3. *Chandra* 0.5–2.0 keV band point source subtracted image, smoothed with a Gaussian full width at half maximum (FWHM) of 3'', overlaid with uGMRT Band 4 radio contours at 20'' resolution (top-panel). *XMM-Newton* image overlaid with LOFAR 144 MHz radio contours at 20'' resolution (bottom-panel). Contour levels are drawn at $[1, 2, 4, 8, \dots] \times 4 \sigma_{\text{rms}}$. The radio beam size is indicated in bottom left corner of the image. The labeling of cold fronts are done following Ge et al. (2020). The overlay shows that the radio halo morphology nicely follows the thermal X-ray emission morphology.

in the radio halo core. Radio emission from the subcomponent is dominated by three bright radio sources (A, B, and C). Deep X-ray studies provide evidence for five discontinuities in X-ray surface brightness: three cold fronts (CF1, CF2, and CF3) and two shock fronts (Ge et al. 2020; Breuer et al. 2020). These

discontinuities (except the northwest shock front) are labeled in Fig. 3.

In the top-right panel of Fig. 4, we show an unsharp-masked *Chandra* image of Abell 2256 obtained with Gaussian smoothing of $\sigma_1 = 4''$ and $\sigma_2 = 40''$. Unsharp-masked maps provide

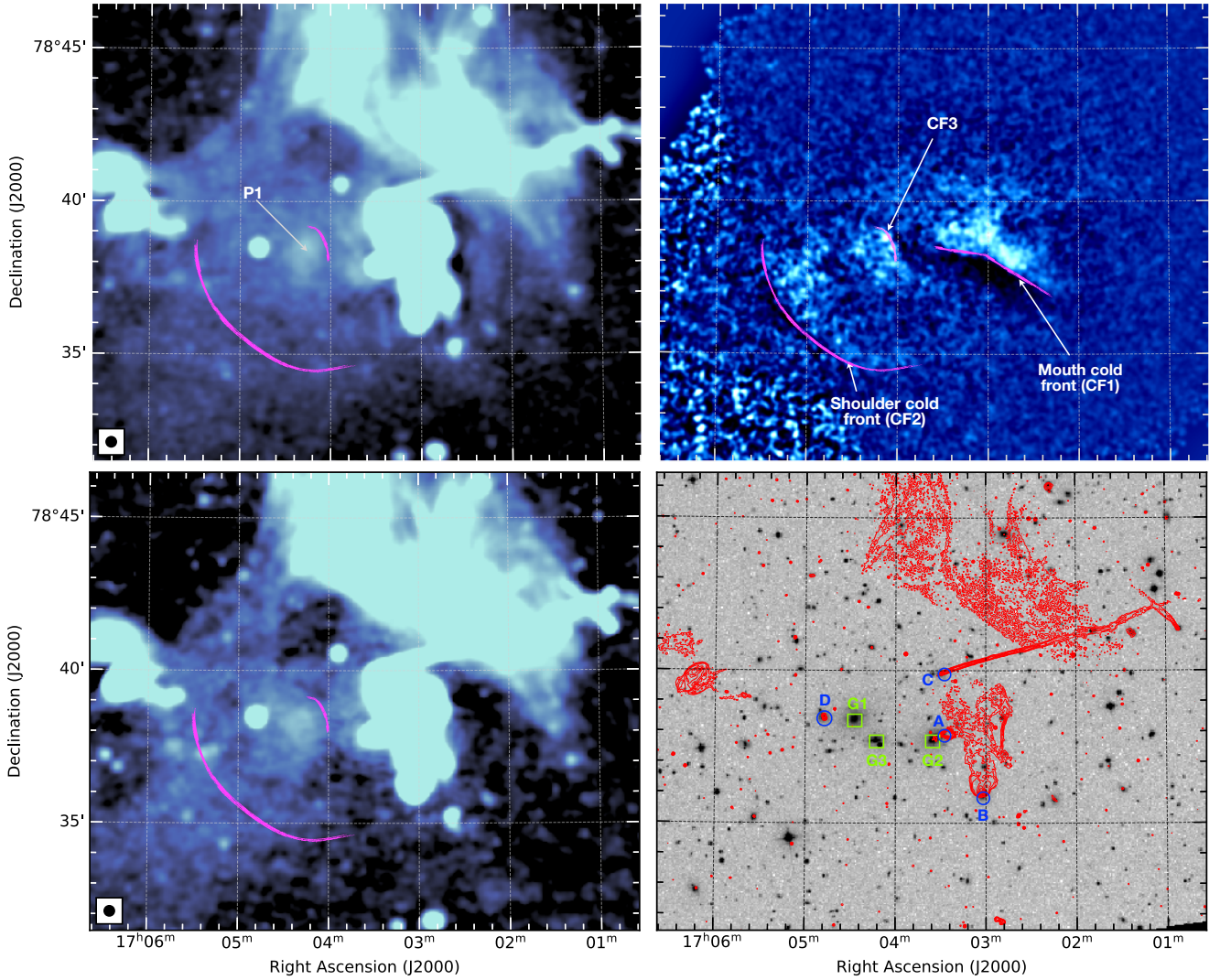


Fig. 4. LOFAR 144 MHz (top-left) and GMRT 350 MHz (bottom-left) image at $20''$ resolution. To compare radio morphologies at these two frequencies, the colors in both images were scaled manually. Unsharp-masked *Chandra* 0.5–2.0 keV image of the cluster A2256 created by subtracting images convolved with Gaussians with σ_1 ($4''$) and σ_2 ($40''$) and dividing by the sum of the two (top-right). The image displays the sharp edges in the X-ray surface brightness image. The labeling of cold fronts (mouth and shoulder) is done following Sun et al. (2002). The comparison of both images reveal that the peak P1 in the radio surface brightness within the main component is confined by the innermost cold front CF1. DSS image overlaid with a high resolution 675 MHz radio contours (bottom-right). Green square boxes and labels mark the bright cluster galaxies in the halo. Blue circles and labels denote the position of known radio galaxies.

a way to investigate the presence of (sharp) discontinuities in the X-ray surface brightness images. The image highlights the presence of three cold fronts (CF1, CF2, and CF3) reported in the inner region of the halo. The positions of these cold fronts are indicated by magenta-colored arcs. It is clear that the bright radio peak P1, in the main component, is confined by the innermost cold front CF3. The morphological similarities between the halo core in radio and X-ray are evident. Source D is an FRI radio source (Fanaroff & Riley 1974), contained within the isophotes of the optical galaxy (Owen et al. 2014). Our new low-frequency images do not show any morphological connection between source D and the halo core. In the inner region of the halo, there are three bright cluster galaxies, namely G1, G2, and G3, see bottom-right panel of Fig. 4. G1 and G3 are located in the main component, but we do not find any radio counterpart in our deep observations but they could have been active in the past and therefore may be providing fossil plasma. Moreover, the peak in the radio emission is

not coincident with G1 or G3. G2 belongs to the subcomponent (Ge et al. 2020).

Recently, Breuer et al. (2020) identified a step-like low-frequency radio surface brightness feature, detected at 325 MHz, that coincides with the long-tail-like X-ray feature (i.e., shoulder cold front see Fig. 4). Compared to Breuer et al. (2020), our low-frequency radio observations are highly sensitive (by a factor of four at about 325 MHz), but we do not find any clear radio feature that coincides with the shoulder cold front. The radio emission indeed shows a step-like morphology but is not really tracing the long X-ray tail.

The emission from the halo extends further to the south, where the X-ray emission is fainter. Recently, Ge et al. (2020) detected a shock front of Mach number $\mathcal{M}_T = 1.54 \pm 0.05$ through a temperature jump at the southern edge of the halo (shown in red in Fig. 3). As mentioned before, in radio maps the southern edge of the halo follows a V-shaped morphology. This V-shaped edge is spatially coincident with the

Table 3. Properties of the halo, wedge arc, and source AI.

Source	LOFAR (144 MHz)	uGMRT (300–850 MHz)		VLA (1–4 GHz)	LLS	$\alpha^{(*)}$
	$S_{144\text{ MHz}}$ (mJy)	$S_{350\text{ MHz}}$ (mJy)	$S_{675\text{ MHz}}$ (mJy)	$S_{1.5\text{ GHz}}$ (mJy)	(Mpc)	
Halo	912 ± 120	217 ± 26	75 ± 8	20 ± 2	~0.77	-1.63 ± 0.03
Wedge arc	150 ± 20	30 ± 7	15 ± 2	3.0 ± 0.5	–	-1.62 ± 0.04
Halo+wedge arc	1062 ± 140	247 ± 33	90 ± 10	23 ± 3	–	-1.63 ± 0.03
AI	41 ± 5	15 ± 2	4.3 ± 0.2	–	~0.46	–

Notes. Flux densities were extracted from 20'' resolution radio maps created with `robust` = -0.5 and an inner uv -cut of 0.1 $k\lambda$. Absolute flux density scale uncertainties are assumed to be 10% for LOFAR and Band3, 5% for uGMRT Band4, and 2.5% for VLA L -band data. The LLS measured at 675 MHz. $(*)$ The integrated spectral index obtained by fitting a single power law fit.

southern shock front in the X-ray image. A similar type of morphology is observed in the case of the Toothbrush cluster (van Weeren et al. 2016), Bullet cluster (Shimwell et al. 2014), Abell 754 (Macario et al. 2011), Coma cluster (Bonafede et al. 2022), and Abell 520 (Markevitch et al. 2005; Vacca et al. 2014).

5. Radio halo analysis

5.1. Integrated spectrum

To obtain the integrated radio spectrum of the halo, we measure flux densities from the 20'' resolution radio images created with a common inner uv -cut of 0.1 $k\lambda$ (here, 0.1 $k\lambda$ is the minimum well-sampled uv -distance in the uGMRT Band 4 data), uv -tapering, and `robust` = -0.5. The region used for measuring the halo flux densities is shown in Fig. 5 (top right). The flux densities of unrelated compact sources were measured manually and subtracted from the total halo flux density. Additionally, the entire region covering sources A, B, and C was excluded. Also, the arc-shaped wedge structure to the east is initially considered a separate structure (discussed in Sect. 5.4).

The resulting integrated spectrum of the halo is shown in the left panel of Fig. 5. The overall spectrum of the halo can be described by a power law. The integrated emission from the halo between 144 MHz and 1.5 GHz has an ultra-steep spectral index of -1.63 ± 0.03 (see Table 3). The halo has a much steeper spectrum than the large relic which shows a spectral index of -1.07 ± 0.02 (Paper I). The steep spectral index of the halo is in agreement with previous studies (Brentjens 2008; van Weeren et al. 2012). There are only a handful of radio halos with such high-sensitivity radio observations over a wide frequency range, namely the halos in MACSJ0717.5+3745 (van Weeren et al. 2017; Rajpurohit et al. 2021a), 1RXSJ0603.3+4214 (van Weeren et al. 2016; Rajpurohit et al. 2018, 2020a), CIZA J2242.8+5301 (van Weeren et al. 2010; Hoang et al. 2017; Di Gennaro et al. 2018), Coma (Bonafede et al. 2022), Abell S1063 (Xie et al. 2020), Abell 2744 (Rajpurohit et al. 2021b), and MACSJ1149.5+2223 (Bruno et al. 2021). Out of these eight (including Abell 2256) radio halos mentioned, most show a spectral index steeper than about -1.4. Three of these halos (Coma, Abell S1063, and MACSJ0717.5+3745) show a high frequency spectral steepening, while the rest follow a single power-law spectrum. Detailed studies of some radio halos with power law spectra have revealed a complex distribution; subregions exhibit different spectral behavior and scattering in the spectral index distribution (Rajpurohit et al. 2021a,b).

Turbulent reacceleration models predict that a significant fraction of the population of radio halos have ultra-steep spec-

trum (e.g., Brunetti et al. 2008). In these models, provided that homogeneous conditions apply in the emitting volume, we expect a spectral steepening at higher frequencies (Cassano et al. 2006). The fact that we do not detect a clear steepening in the integrated spectrum of the Abell 2256 halo may imply that the emitting volume is not homogeneous. Perhaps the subregions of the halo show different spectral behavior, but the overall spectrum results in the power-law behavior, as recently reported for the halo in Abell 2744 (Rajpurohit et al. 2021b).

To investigate this, we divide the halo into four subregions, core, region1, region2, and region3. These regions are shown in the bottom right panel of Fig. 5: the core is the innermost region and region3 the outermost. The regions that are masked are shown in magenta. The resulting spectra are shown in Fig. 5 (bottom left panel). The subregions of the halo show different spectral slopes. The core can be well described by a power law spectrum with slope -1.60. The spectrum of region2 can also be described by a power law with slope -1.44. The core region is steeper compared to region2. There is a clear high frequency steepening in region1 and region3. This implies that a general power-law emission spectrum, observed for many halos, does not necessarily imply that electrons have everywhere in the halo the same power-law distribution (Rajpurohit et al. 2021b).

Excluding the core region, it is clear that there is a radial steepening in the halo when moving to larger radii. The synchrotron frequency (or steepening) in the turbulent reacceleration model (Cassano & Brunetti 2005) is given by:

$$\nu_s \propto \frac{\tau_{\text{acc}}^{-2} B}{(B^2 + B_{\text{cmb}}^2)^2}, \quad (2)$$

where B is the magnetic field and τ_{acc} is the minimum acceleration time in the emitting volume. Therefore, a radial steepening is expected from the decline of the magnetic field (for constant τ_{acc}), at least at large distances where presumably $B < B_{\text{cmb}}/\sqrt{3}$ or due to a decline of τ_{acc}^{-2} (i.e., less acceleration at larger distances). However, this assumes that local conditions change only as a function of radius.

5.2. Radio power versus mass relation

Using the flux densities measured at 1.5 GHz and 144 MHz, we estimate the total radio power of the halo. We note that the wedge arc is also considered part of the halo. The total rest-frame radio powers of the halo are $P_{1.4\text{ GHz, lower limit}} = (1.9 \pm 0.2) \times 10^{23} \text{ W Hz}^{-1}$ and $P_{150\text{ MHz, lower limit}} = (8.9 \pm 0.8) \times 10^{24} \text{ W Hz}^{-1}$. Our new measurement of the halo yields a 1.4 GHz radio power that is at least 4 times lower than previously reported from

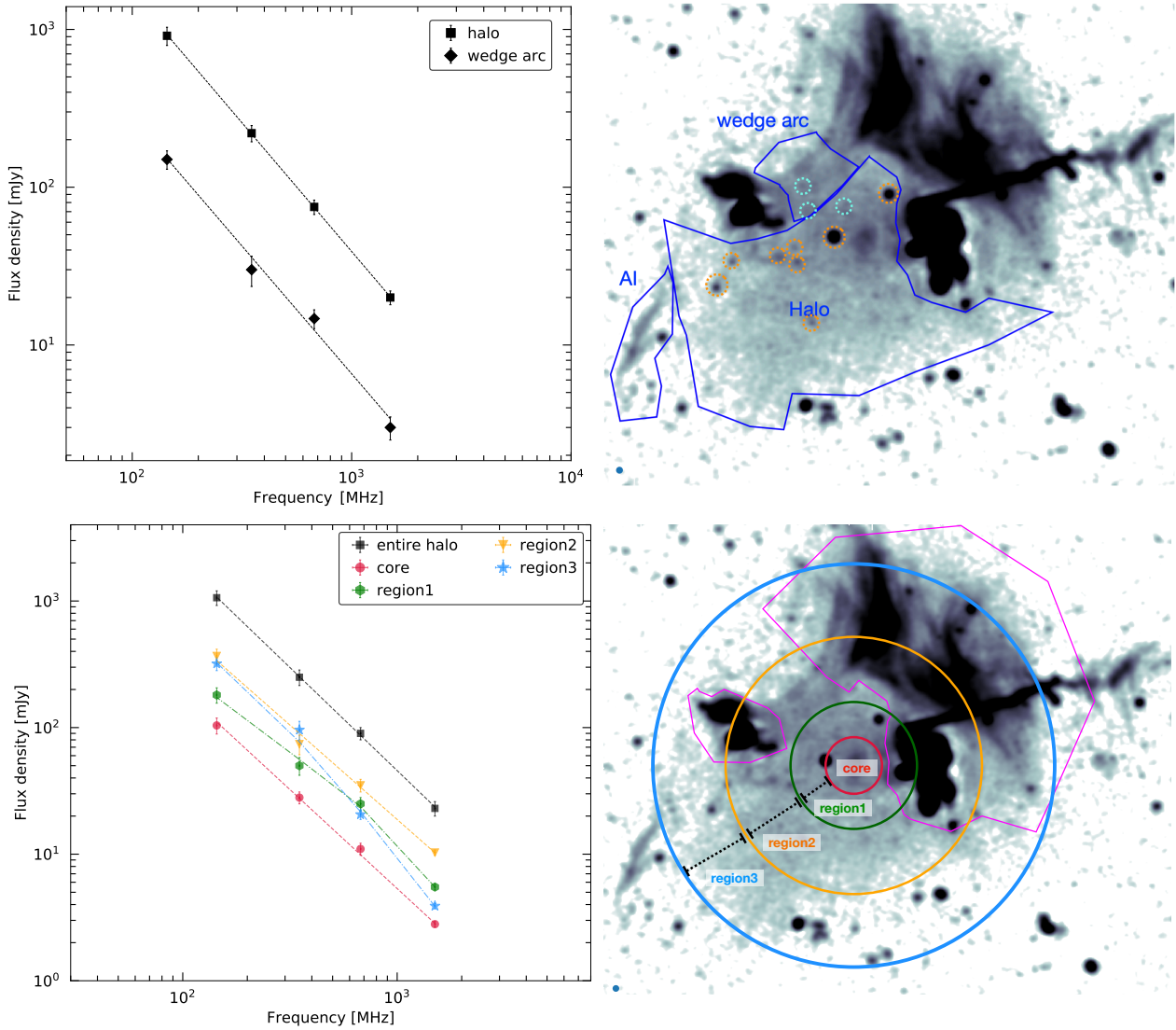


Fig. 5. Integrated spectrum of the radio halo and the wedge arc between 144 MHz and 1.5 GHz (top-left). Dashed lines show the fitted power law. The overall spectrum of the halo follows a single power law and has an ultra-steep spectral index of -1.63 ± 0.03 . The halo subregions spectra, showing different spectral indices (bottom-left). Dashed lines show the fitted power law and dot-dashed fitted with curved spectra. LOFAR 144 MHz image overlaid with regions used for extracting flux densities of the halo, wedged arc and source AI (top-right). Flux density contributions from compact sources (shown with dashed circles) were manually subtracted from the total halo flux density. Cyan circles denote compact sources that are detected in the uGMRT and VLA images. The halo subregions: core is the innermost part and region3 the outermost one (bottom-right). These regions are used for extracting the flux densities and the radio and X-ray surface brightness in the halo subregions. Magenta polygons depict masked regions, that is not included for measuring the halo flux densities.

Clarke & Ensslin (2006), namely $8.2 \times 10^{23} \text{ W Hz}^{-1}$. We note that Clarke & Ensslin (2006) used a larger and different area for the measurement of the flux density. Moreover, their flux density value may be affected by unresolved unrelated sources.

The radio halo is very likely seen in projection with sources A, B, and C, so the above estimated radio power provides a lower limit. Moreover, part of the halo emission could be seen in projection with the relic. However, the large-scale structure of Abell 2256 makes it very difficult to determine the exact northern boundary of the halo. As discussed in Sect. 4.2, the radio halo morphology nicely traces the X-ray morphology. Therefore, we take the northwest boundary of the halo using the X-ray distribution at that location. To estimate the upper limit of the halo power, we extrapolated the halo flux density in the area covering sources A, B, C, and the northwest part of the relic by using the average flux from the halo per unit surface area outside that

region. In this way, the total halo flux density values at 144 MHz and 1.5 GHz are 1570 mJy and 36 mJy, respectively. This gives the radio power of $P_{1.4\text{GHz, upper bound}} = 3.1 \times 10^{23} \text{ W Hz}^{-1}$ and $P_{150\text{MHz, upper bound}} = 1.3 \times 10^{25} \text{ W Hz}^{-1}$. We also checked the halo flux density using the halo-FDCA package (Boxelaar et al. 2021) and the resulting values are comparable (Osinga et al. in prep.).

It is well known that the radio power (at 1.4 GHz and 150 MHz) of halos show a well defined correlation with the mass and X-ray luminosity of the host cluster (Cassano et al. 2013; van Weeren et al. 2021; Duchesne et al. 2021; Cuciti et al. 2021). With our new radio power (considering upper bound), the halo in Abell 2256 is a factor of 4 below this correlation at 1.4 GHz (Cuciti et al. 2021). The halo falls into the category of underluminous halos in the known 1.4 GHz radio power versus mass relation (Cassano et al. 2013). To

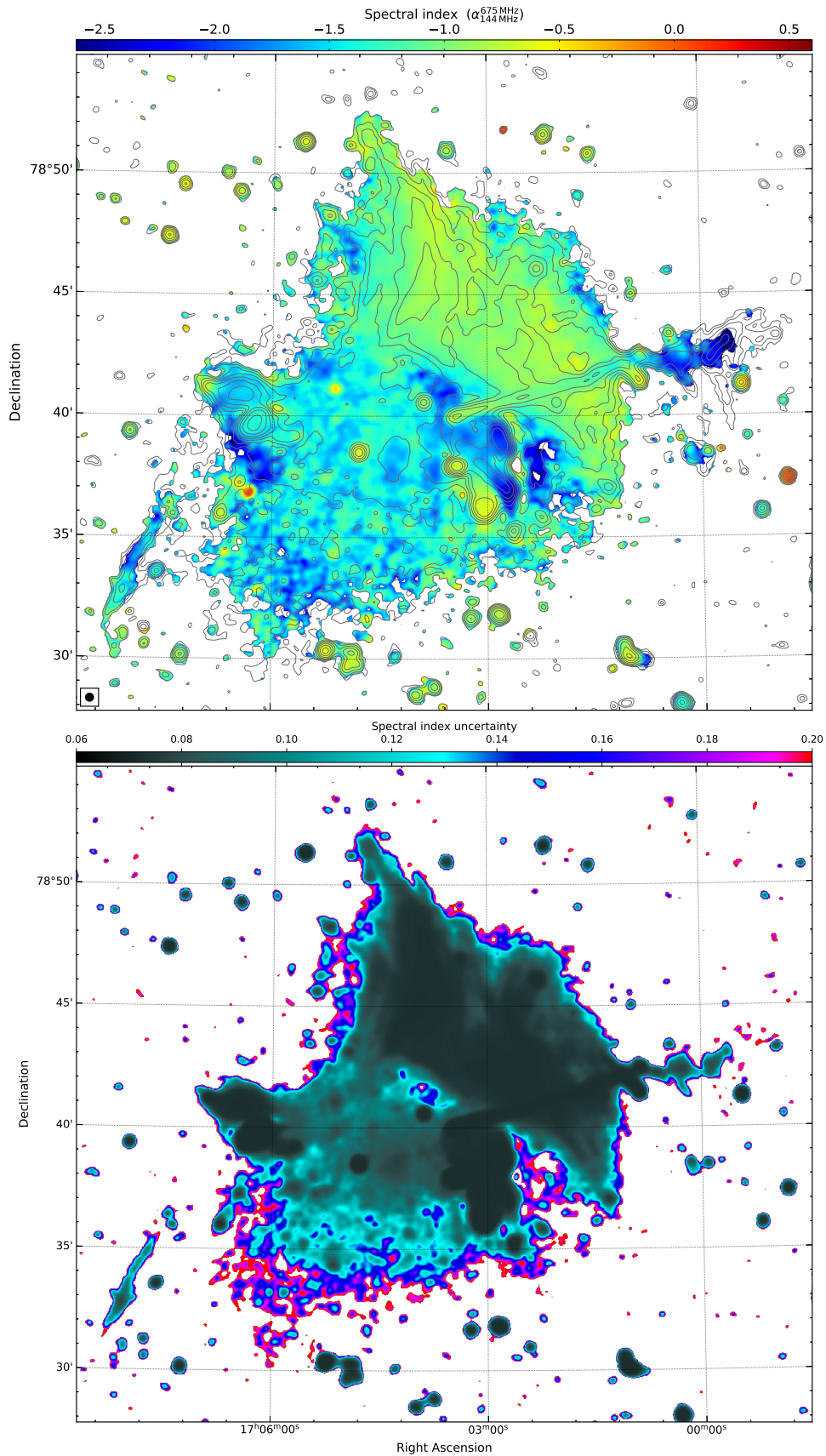


Fig. 6. Spectral index map of the halo at 20'' resolution between 144 and 675 MHz (top). The halo spectral index varies on the scale of about 20 kpc. Contour levels are drawn at $[1, 2, 4, 8, \dots] \times 3.0 \sigma_{\text{rms}}$ and are from the LOFAR 144 MHz image. Corresponding spectral index uncertainty (bottom). The beam size is indicated in the bottom left corner of the image.

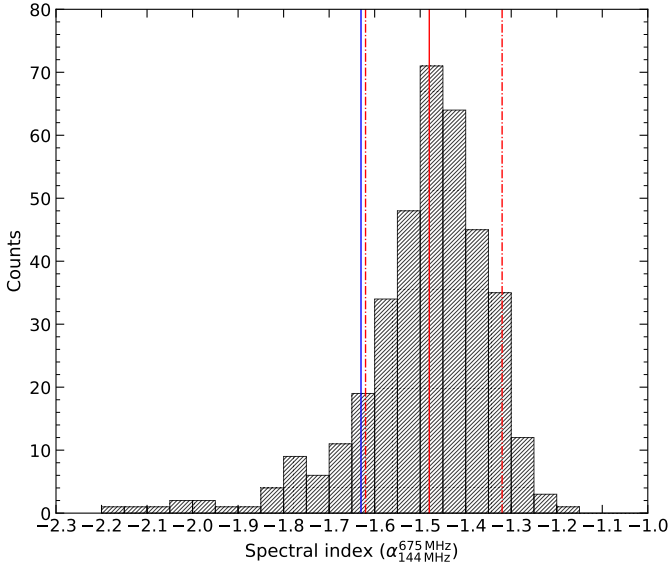


Fig. 7. Histogram of the spectral index distribution across the halo in Abell 2256 between 144 MHz and 675 MHz. The spectral indices were extracted from square-shaped boxes with width $20''$, corresponding to a physical size of about 23 kpc. The solid red line represents the median spectral index, namely $\langle\alpha\rangle = -1.48$. The dash dotted lines show the standard deviation around the median spectral index, $\sigma = 0.16$. The blue line indicates the integrated spectrum of the halo.

the best of our knowledge, underluminous radio halos are also reported in Abell 1451 (Cuciti et al. 2018), ZwCl0634+47 (Cuciti et al. 2018), Abell 1430 (Hoeft et al. 2021), Abell 3667 (de Gasperin et al. 2022), Abell 1689 (Vacca et al. 2011), Abell 2218 (Giovannini & Feretti 2000), and Abell 3266 (Riseley et al. 2022a). We emphasize that, compared to these known underluminous halos, the one in Abell 2256 has a reliable characterization of its spectrum. Moreover, the radio power of halos at 1.4 GHz scales with the X-ray luminosity of the hosting clusters. Ultra-steep spectrum radio halos are expected to be underluminous with respect to this correlation (Cassano 2010). Moreover, MHD simulations suggest that during the formation and evolution of the halos, the halo can be underluminous or luminous (Donnert et al. 2013): steep spectrum radio halos in the very early or very late stages of their lifetimes are expected to be underluminous. This scenario seems plausible for the radio halo in Abell 2256 due to its ultra-steep spectrum and low radio power at 1.4 GHz. Similar to the radio power vs. mass relation, the Abell 2256 halo is underluminous also in the radio power vs. X-ray luminosity relation. In contrast to the radio power versus mass relation at 1.4 GHz, the halo fits well in the radio power versus mass relation at 150 MHz (van Weeren et al. 2021; Duchesne et al. 2021). This hints that these correlations are frequency-dependent.

5.3. Spectral index distribution

To check the spectral variations in the halo, we construct a spectral index map of the halo between 144 MHz and 675 MHz using the $20''$ resolution images described in Sect. 5.1. Since the total extent of the halo decreases at high frequencies, which in turn significantly reduces the area over which we can study the spectral index distribution, we do not use 1.5 GHz data. Pixels with flux densities below $3\sigma_{\text{rms}}$ at both frequencies were blanked.

In the top panel of Fig. 6, we show the spectral index map of the halo emission between 144 MHz and 675 MHz. Excluding unrelated sources, the spectral index, across the halo, varies between -1.3 and -1.8 . The core is evidently steep (-1.65) compared to the surrounding region. This value is consistent with the overall spectrum of the core region. It is plausible that the bright steep core is associated with the previous AGN activity. Thus its spectrum is affected by the external halo emission seen in projection. This would imply that the core spectrum is even steeper than observed (-1.60), since true region 1 is projected on the core. We note that in case the halo core is related to an old AGN lobe, we expect a curved spectrum. In contrast, the halo core follows a power-law spectrum between 144 MHz and 1.5 GHz.

In Fig. 7, we show a histogram of the spectral index in the halo. The distribution is asymmetric, showing a median value of $\langle\alpha\rangle = -1.48$ and a standard deviation of $\sigma = 0.16$. If the variations in the spectral index are the result of measurement errors, we expect the median error value to be comparable to the standard deviation. For the halo, we find a median error of 0.08. This value is about a factor of 2 smaller than the standard deviation, which implies that there are intrinsic small-scale fluctuations in the spectral index across the halo. Fluctuations in the spectral index are also reported for the halos in Abell 2255 (Botteon et al. 2020a), Abell 520 (Hoang et al. 2019), MACS J0717.5+3745 (Rajpurohit et al. 2021a), and Abell 2744 (Rajpurohit et al. 2021b). We emphasize that the fluctuations in the spectral index of the Abell 2256 halo again highlights the contradiction with the overall spectrum, which is a power law. The spatially resolved spectral index map shows a mean spectral index of -1.50 , which is slightly flatter than the one obtained from the integrated spectrum. However, this is expected since the halo is more extended at 144 MHz and in those regions the radio surface brightness is below $3\sigma_{\text{rms}}$ at 675 MHz, thus not included in Fig. 5. Moreover, the integrated spectrum is brightness weighted, while in the spectral index map each pixel has the same relevance, regardless of its brightness (i.e., signal-to-noise ratio).

5.4. Radio versus X-ray surface brightness

Radio halos often show a point-to-point correlation between radio and X-ray surface brightness (Govoni et al. 2001a,b; Shimwell et al. 2014; Rajpurohit et al. 2018, 2021a,b; Hoang et al. 2019, 2021; Cova et al. 2019; Xie et al. 2020; Botteon et al. 2020b; Bruno et al. 2021; Duchesne et al. 2021; Bonafede et al. 2022; Riseley et al. 2022a). The correlation slope is mostly found to be sublinear in radio halos, that is the nonthermal radio emission declines less rapidly than the thermal X-ray emission. Relatively few radio halos have high-quality multifrequency radio data available. Of these halos, a few show that the correlation slope changes as a function of frequency (Rajpurohit et al. 2021a; Hoang et al. 2021). However, there is also a case where the correlation slope remains constant as a function of frequency, the halo in Abell 2744 (Rajpurohit et al. 2021b).

We check whether there is any correlation between the X-ray and radio surface brightness for the halo in Abell 2256. We used $20''$ resolution radio maps at 144 MHz, 675 MHz, and 1.5 GHz. For X-ray, we used an *XMM-Newton* 0.5–2 keV image smoothed with a Gaussian of $6''$ FWHM. First, we create a grid (with square boxes of width $20''$) that covers the halo region visible at all three frequencies, including the wedge arc. We exclude areas with discrete radio and X-ray point sources. We include regions

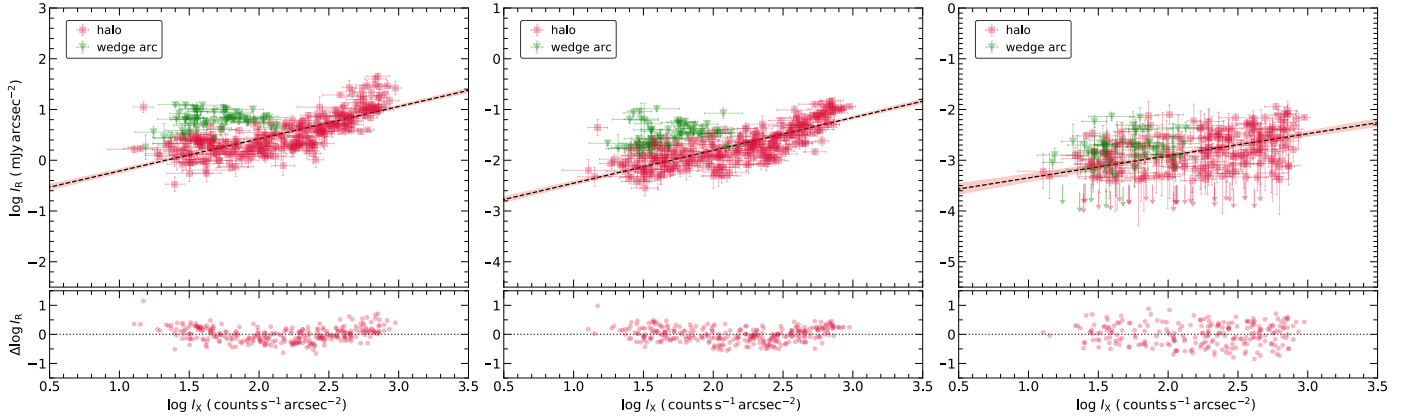


Fig. 8. Radio versus X-ray surface brightness correlation for the halo in Abell 2256 at 144 MHz (Left), 675 MHz (Middle), and 1.5 GHz (Right). The surface brightness is extracted from square-shaped boxes (width of 23 kpc) and in a “common region” visible across all three frequencies. The X-ray surface brightness is extracted from the *XMM-Newton* (0.5–2 keV band) image smoothed with a Gaussian FWHM of 6” to have a good signal-to-noise ratio in the fainter outer regions. The radio surface brightness is extracted from radio maps at 20” resolution. The *Linmix* best-fit relations for the halo data points are depicted as black dashed lines. Squared-shape boxes represent cells where both the radio and X-ray surface brightness is greater than 3σ . The 2σ upper limits are indicated by arrows. The lower panel shows the residuals of $\log I_R$ and $\log I_X$ with respect to the *Linmix* best fit line for the halo region only. Green data points are extracted from the wedge arc.

Table 4. *Linmix* fitting slopes and Spearman (r_s) and Pearson (r_p) correlation coefficients of the data for Figs. 8 and 9.

	ν	3σ				2σ as upper limits			
		b	σ_{int}	r_s	r_p	b	σ_{int}	r_s	r_p
Halo (common region)	144 MHz	0.64 ± 0.02	0.08 ± 0.01	0.79	0.76	0.64 ± 0.02	0.08 ± 0.01	0.79	0.76
	675 MHz	0.64 ± 0.03	0.05 ± 0.01	0.81	0.76	0.65 ± 0.03	0.05 ± 0.01	0.81	0.76
	1.5 GHz	0.37 ± 0.05	0.07 ± 0.01	0.55	0.39	0.44 ± 0.05	0.07 ± 0.05	0.54	0.39
Halo+wedge arc (common region)	144 MHz	0.43 ± 0.03	0.09 ± 0.01	0.56	0.54	0.43 ± 0.03	0.09 ± 0.01	0.56	0.54
	675 MHz	0.44 ± 0.03	0.08 ± 0.01	0.60	0.56	0.44 ± 0.03	0.08 ± 0.01	0.60	0.56
	1.5 GHz	0.28 ± 0.04	0.07 ± 0.01	0.46	0.33	0.33 ± 0.04	0.07 ± 0.01	0.46	0.27
Halo	144 MHz	0.60 ± 0.01	0.06 ± 0.01	0.89	0.86	0.70 ± 0.02	0.15 ± 0.01	0.87	0.85
	675 MHz	0.60 ± 0.02	0.05 ± 0.01	0.87	0.80	0.72 ± 0.02	0.08 ± 0.01	0.88	0.84
	1.5 GHz	0.37 ± 0.05	0.07 ± 0.01	0.55	0.39	0.44 ± 0.05	0.07 ± 0.05	0.54	0.39
Halo+wedge arc	144 MHz	0.61 ± 0.02	0.09 ± 0.01	0.83	0.80	0.73 ± 0.02	0.15 ± 0.01	0.82	0.80
	675 MHz	0.57 ± 0.02	0.08 ± 0.01	0.80	0.70	0.73 ± 0.02	0.12 ± 0.01	0.83	0.79
	1.5 GHz	0.28 ± 0.04	0.07 ± 0.01	0.46	0.33	0.33 ± 0.04	0.07 ± 0.01	0.46	0.27

where the radio and X-ray surface brightness is above the 2σ level. The emission below 3σ is included as upper limits.

The resulting plots at 144 MHz, 675 MHz, and 1.5 GHz are shown in Fig. 8. Despite the complex distribution of the thermal and nonthermal emission components at the center, there seems to be a positive correlation between the radio and X-ray surface brightness for all three frequencies: higher radio brightness is associated with higher X-ray brightness. To check the strength of the correlation, we fit the data with a power law of the form

$$I_R \propto I_X^b, \quad (3)$$

where b is the correlation slope. We use the *Linmix* package (Kelly 2007) for fitting. The Spearman correlation coefficients at the observed frequencies are $r_{s,144\text{MHz}} = 0.56$, $r_{s,675\text{MHz}} = 0.60$, and $r_{s,1.5\text{GHz}} = 0.46$. There is a moderate correlation between the two quantities, but it is weak at 1.5 GHz. The correlation slope is sublinear and more or less constant at 144 MHz and 675 MHz, namely $b_{144\text{MHz}} = 0.43 \pm 0.03$ and $b_{675\text{MHz}} = 0.44 \pm 0.03$.

When excluding the wedge arc, we find that for the rest of the data points, the radio and X-ray surface brightness is correlated at

Table 5. *Linmix* correlation slope within the halo subregions of Fig. 10.

	Slope (b)	Correlation coefficient (r_s)
Core	1.51 ± 0.32	0.64
region1	0.71 ± 0.09	0.56
region2	0.99 ± 0.07	0.61
region3	0.41 ± 0.09	0.18

144 MHz and 675 MHz with correlation coefficient of $r_{s,144\text{MHz}} = 0.79$ and $r_{s,675\text{MHz}} = 0.81$, respectively. At high frequencies, the correlation is comparatively weak, namely $r_{s,1.5\text{GHz}} = 0.54$. Similar to other known halos, the correlation slope is sublinear in the Abell 2256 halo, see Table 4. However, unlike other halos, the correlation slope is flatter at high frequencies. Similar trends are observed for the halos in CLG 0217+70 (Hoang et al. 2021) and Abell 520 (Hoang et al. 2019). For the halo in CLG 0217+70, a flat correlation slope at high frequency is caused by X-ray surface brightness discontinuities at the edges of the halo that indicate regions where reacceleration take place.

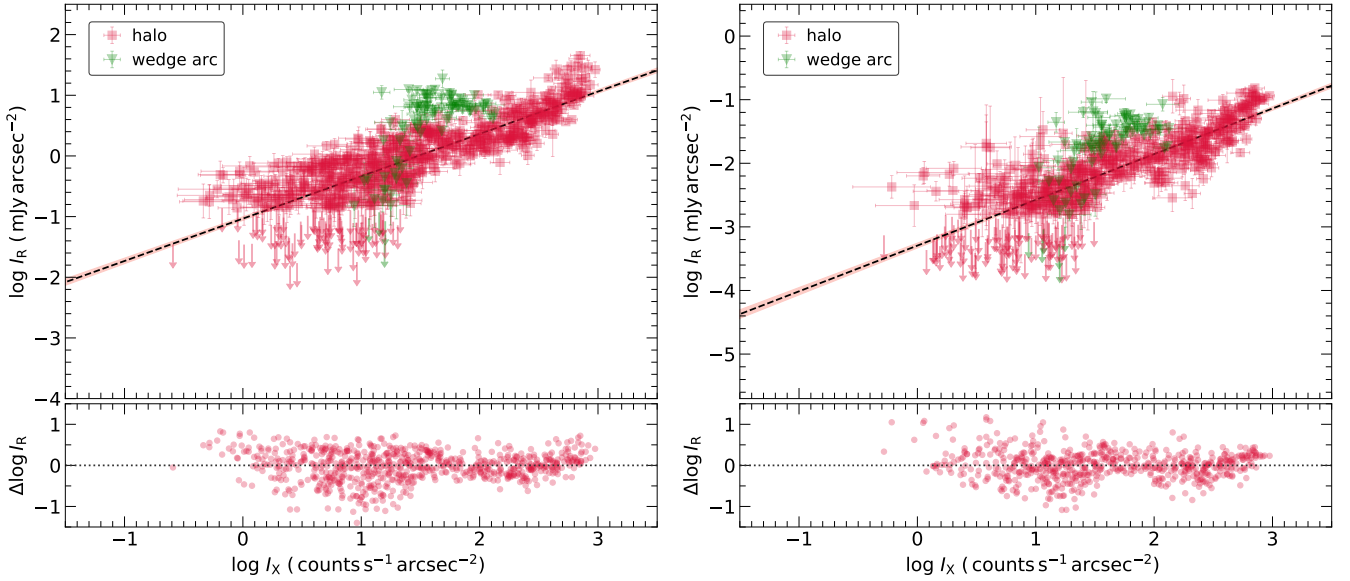


Fig. 9. Radio versus X-ray surface brightness correlation for the halo in Abell 2256 at 144 MHz (left) and 675 MHz (Right). Images and fitting is the same as in Fig. 8 but including all regions where both radio and X-ray surface brightness exceeds 2σ (emission below 3σ is shown as upper limits). Correlation between the radio and X-ray surface brightness across the halo region gets tighter when including all the halo emission at low frequencies. The best-fitted correlation slopes are $b_{144\text{MHz}} = 0.87 \pm 0.02$, $b_{675\text{MHz}} = 0.88 \pm 0.03$ in the halo region. The data points from the wedge arc are not scattered but are above the halo correlation.

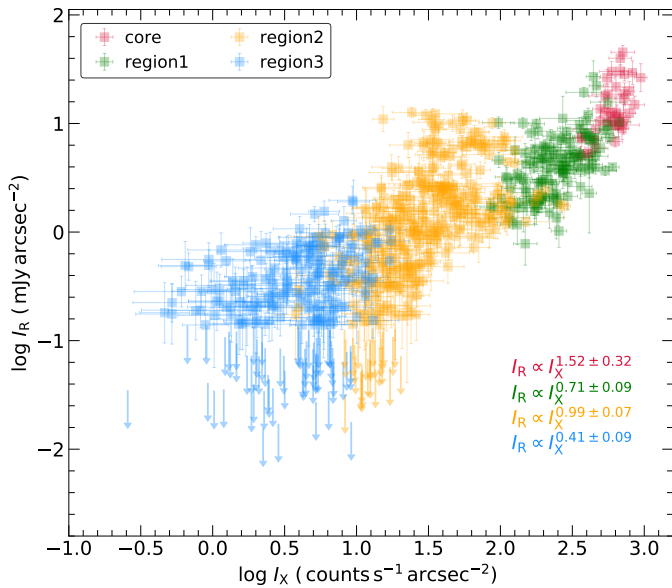


Fig. 10. Radio versus X-ray surface brightness distribution at 144 MHz (similar to Fig. 9 left panel) in the inner and outer regions of the halo; color coded with different circles (see Fig. 5 bottom right panel). Blue and green circles (region3) covers the outermost region while the core that of the innermost region of the halo. The subregions of the halo show different correlation slopes.

Four X-ray surface brightness edges have been reported within the halo in Abell 2256 (Ge et al. 2020). Three of them are cold fronts detected in the inner regions, whereas the fourth is a shock front found to the southeast of the halo. When considering the data points of the wedge arc as a part of the halo, the radio versus X-ray correlation is not that strong at all three frequencies; see Table 4. As shown in Fig. 8, the data points from the wedge arc are mostly clustered above the correlation (in particular at 144 MHz and 675 MHz) and the correlation is

moderate when considering only the region of the halo visible at all frequencies. However, when including the entire halo emission, that is the radio emission $>3\sigma$ level (2σ as upper limits) at 144 MHz and 650 MHz, there is a strong correlation. We emphasize that the data points from the wedge arc lie above the correlation but do not scatter significantly from the halo data points (see Fig. 9). Moreover, the correlation slope is more or less the same with and without the wedge arc.

As the total extent of the halo emission is large below 1.5 GHz, we created another grid that covers the entire halo region ($>3\sigma$) at 144 MHz and 675 MHz. The resulting plots are shown in Fig. 9. In these plots, a large region with less dense X-ray regions can be seen. Moreover, compared to Fig. 8, there is a strong correlation between radio and X-ray surface brightness with a correlation coefficient of $r_{s,144\text{MHz}} = 0.88$ and $r_{s,675\text{MHz}} = 0.87$.

Following Bonafede et al. (2022), we study the correlation of radio and X-ray surface brightness in the inner and outer regions of the halo. Since the halo is more extended toward low frequencies, we use the LOFAR 144 MHz map to measure the radio surface brightness. We repeat the analysis described above, that is extract the radio and X-ray surface brightness within square-shaped boxes of size 23 kpc but this time in the subregions: core, region1, region2, and region3. The resulting plot is shown in Fig. 10. We find that the halo slope changes drastically from the core to region3, see Table 5. Within the core region, the correlation slope is 1.51 ± 0.32 while in the outermost region (region3) 0.41 ± 0.09 . The slopes for region1 and region2 are 0.71 ± 0.09 and 0.99 ± 0.07 , respectively. This indicates that the slope is superlinear in the halo core and sublinear in the outermost fainter region. It is worth noticing that the opposite trend has been found for the halo in the Coma cluster (Bonafede et al. 2022), possibly highlighting different physical conditions in these two systems. A superlinear slope is found in the inner region followed by flattening in the outermost region for some cool core clusters that host a hybrid halo, that is, a mini halo and halo-type component, for example in RXC J1720.1+2638 (Biava et al. 2021), MS

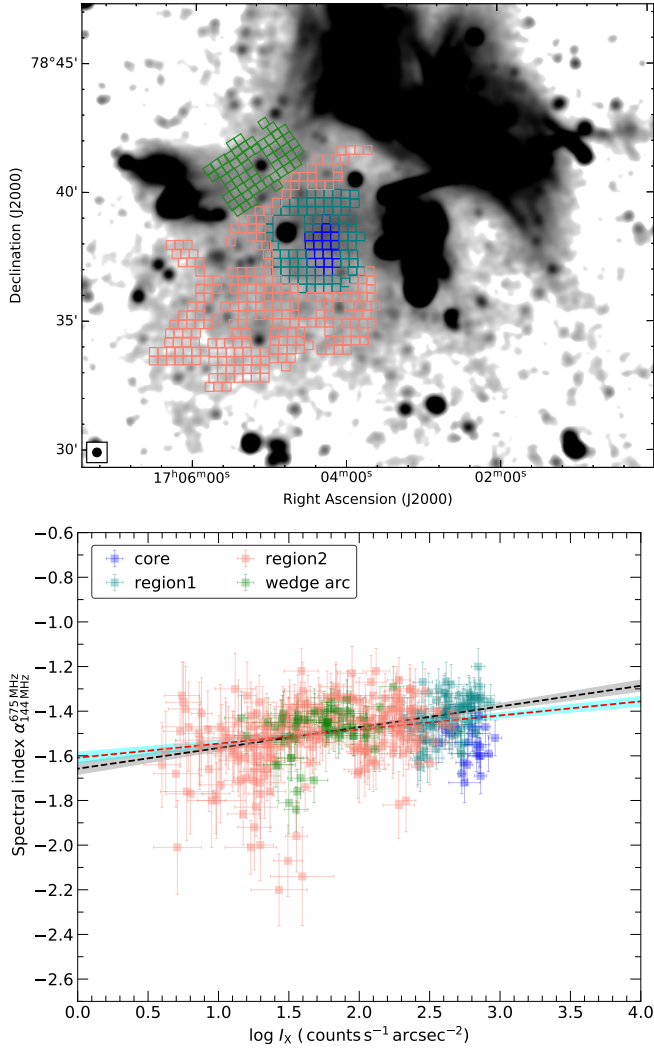


Fig. 11. Regions used to obtain the $\alpha - I_X$ correlation (top). The radio spectral index values were extracted between 144 MHz and 675 MHz. Each box has a width of $20''$ corresponding to a physical size of about 23 kpc. The spectral index versus X-ray surface brightness relation across the halo in Abell 2256 (bottom). There is a strong anticorrelation between these two quantities (the black dashed line shows the fitting excluding the core region while the red dashed line includes the core region).

1455.0+2232 (Riseley et al. 2022b), and Abell 1413 (Lusetti et al, in prep.). We emphasize that there is no systematic trend in the correlation slope for the halo in Abell 2256 as we move toward the outer regions. The presence of different slopes in the halo subregions (core, region1, region2, and region3) can be induced by several processes and their interplay, as discussed in Sect. 5.6.

5.5. Spectral index versus X-ray surface brightness

We also check the point-to-point relation between the spectral index and the X-ray surface brightness for the halo in Abell 2256. We divided the halo into three different regions: the core, innermost, and outermost regions (see Fig. 11 top panel). The data points associated with the wedge arc are also considered separately. To have high signal-to-noise ratio, we only included regions where radio (at 144 and 675 MHz) and X-ray surface brightness have emission above $3\sigma_{\text{rms}}$. The resulting plot is

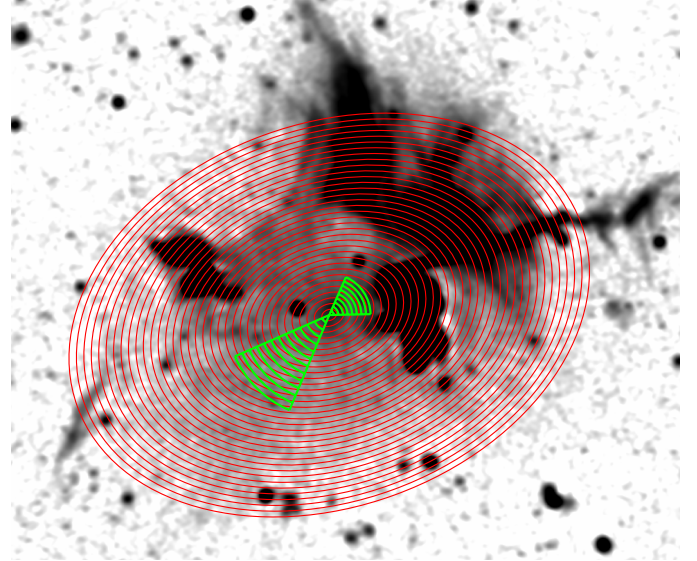


Fig. 12. LOFAR 144 MHz radio image of the Abell 2256 cluster at $20''$ resolution overlaid with the red ellipse (with a major axis radius of 700 kpc) that is used to extract radial profiles shown in Fig. 13. The green sectors show the radial profiles extracted across the cold front CF2 and CF3. The width of the each annulus is 23 kpc.

shown in the bottom panel of Fig. 11. There seems to be an anticorrelation between these two quantities: the fainter X-ray regions show the steepest spectral index. We again fit the data with a power law. The Spearman correlation coefficient is about -0.60 ± 0.10 . Therefore, there is a moderate anticorrelation between the spectral index and the X-ray surface brightness.

Most of the X-ray emission is produced by the core in the main component of the cluster, where the radio spectral index is rather steep. It is plausible that the ICM and magnetic field in the core region has been moderately perturbed and stirred. It is indeed possible that the dense core region is more shielded by gas dynamics during the merger and thus is less turbulent. This may explain why the spectral index measured in the core region is that steeper and also the fact that the overall point-to-point radio-to-X-ray surface brightness correlation is quite superlinear in the core region. If we exclude the core region of the cluster, the $\alpha - I_X$ relation shows a strong correlation with the Spearman correlation coefficient of -0.88 ± 0.07 (slope $b = 0.09 \pm 0.01$), see bottom panel of Fig. 11.

To our knowledge, the correlation between the spectral index and X-ray surface brightness has been studied so far only for four radio halos, with good statistical significance, namely in MACS J0717.5+3745, Abell 2255, Abell 2744, and CIG 0217+70. In MACS J0717.5+3745 and Abell 2255 halos, a negative and positive correlation, respectively, have been found between these two quantities (Rajpurohit et al. 2021a; Botteon et al. 2020a). In contrast, for the halo in A2744, both positive and negative correlations have been reported, indicating a multicomponent halo (Rajpurohit et al. 2021b), while no significant correlation was found for the halo in CLG 0217+70 (Hoang et al. 2021).

5.6. Radial profiles

In order to investigate any connection between the radio emission and X-ray discontinuities, we created radial profiles using radio and X-ray maps. The mean of the radio and X-ray surface

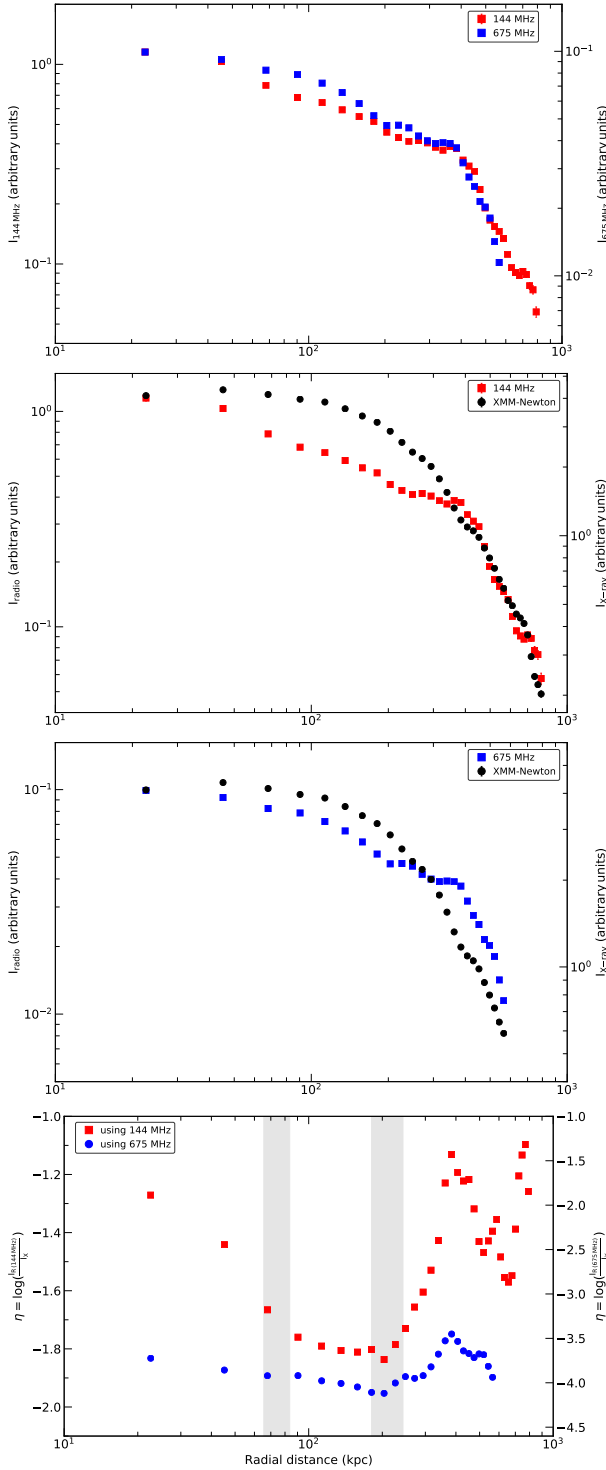


Fig. 13. Radial profiles extracted from radio and X-ray maps. The 144 MHz and 675 MHz profiles seem more or less similar (Top panel). However, the radio profiles seem steeper than the X-ray (Middle panels). The bars represent only statistical errors and do not appear because they are smaller than the data points. The η profile (Bottom panel) extracted by dividing radio (144 MHz and 675 MHz) and X-ray surface brightness. The gray-shaded areas show the location of cold fronts (CF3 and CF2). The region used for extracting the profiles is shown with red in Fig. 12.

brightness and its errors were computed within concentric elliptical annuli, each having a width of $20''$, that is the beam size of the radio maps. The annuli used are shown in Fig. 12. The

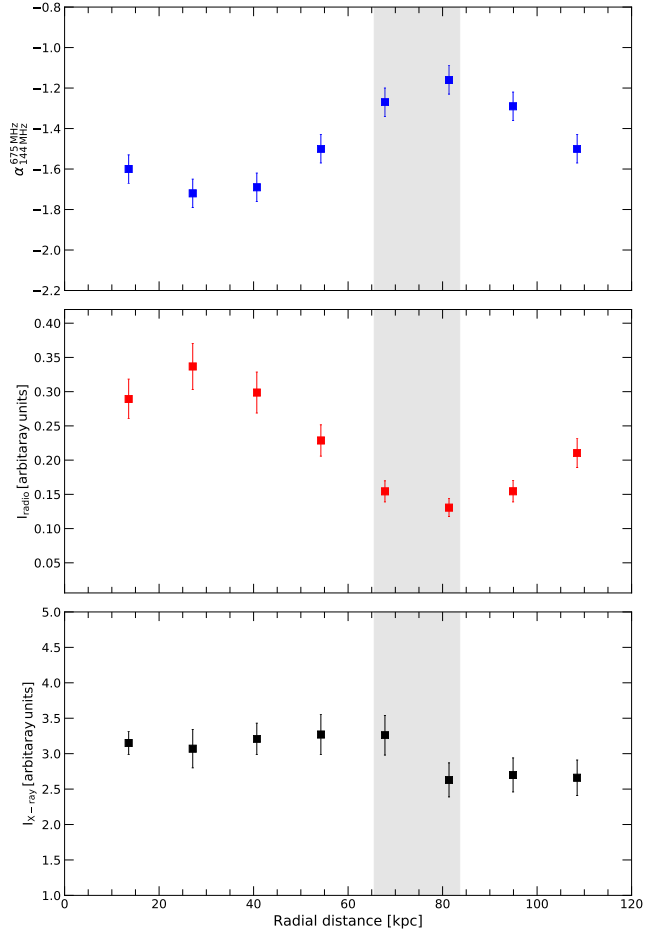


Fig. 14. Spectral index (top), radio (middle) and X-ray (bottom) surface brightness profiles at the cold front CF3 (shown with gray shaded region). The width of each annulus is $12''$. The error bars represent both statistical and flux density scale errors. Both radio and X-ray profiles show a jump at the cold front.

area containing the relic and sources A, B, C, and F (magenta regions in Fig. 5 bottom right panel) was not included in both radio and X-ray profiles. Moreover, other additional unrelated compact sources were also excluded; we simply masked them. We only included regions where the radio and X-ray surface brightness exceeds 3σ . The resulting plot is shown in Fig. 13. In this plot, the halo is about 0.8 Mpc in diameter at 144 MHz only. The top panel shows the comparison of the radial profiles at 144 and 675 MHz. Radio radial profiles at these two frequencies follow more or less the same trend and decline sharply after 450 kpc. The innermost regions (<450 kpc radii) are relatively flat. Typically, radio halos brightness profiles are described by an exponential law of the form

$$I_r = I_0 e^{-\frac{r}{r_e}}, \quad (4)$$

where I_0 is the central radio brightness and r_e is the e-folding radius (Murgia et al. 2009; Bonafede et al. 2022). The halo in Abell 2256 shows a convex $\log(I)$ profile in the innermost regions (between 100 – $350''$) instead of a concave profile, as observed for other known halos, for example Coma (Bonafede et al. 2022), Abell 2744 (Orú et al. 2007; Murgia et al. 2009; Pearce et al. 2017), and Abell 2255 (Murgia et al. 2009). Mini halos, that often host a central BCG, are known to show a convex profile in the innermost region (Murgia et al. 2009; Riseley et al. 2022b). We emphasize that the

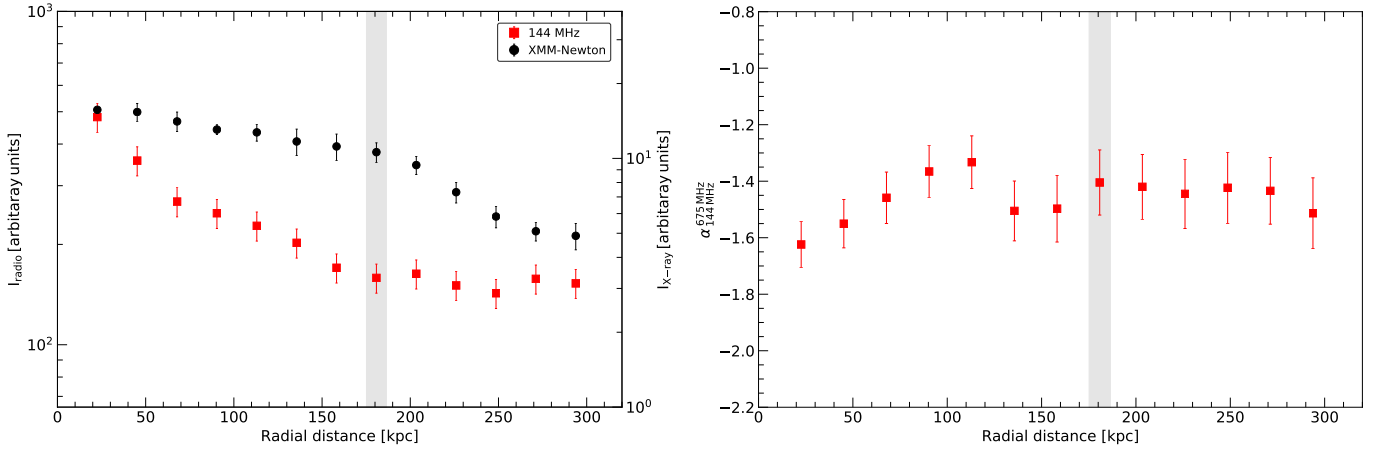


Fig. 15. Radio (left) and spectral index (right) profiles extracted in a sector at the cold front CF2 (shown with gray shaded region). Sector used for extracting the profile across CF2 is shown in Fig. 10. The width of each annulus is $20''$. The error bars represent both statistical and flux density scale errors. Both radio and X-ray profiles show a jump at the cold front CF2. The sector used for extracting these profiles are shown in Fig. 12. The gray shaded area for CF2 is smaller than the one shown in Fig. 13 because CF2 extends over various radii (shown in red in Fig. 12) but in the current Figure the sector used for flux extraction is smaller (green sector in Fig. 12), that is smaller than the actual cold front length.

core region of the halo in Abell 2256 is apparently not associated with any clear radio galaxy.

The comparison of X-ray and radio profiles is shown in Fig. 13 middle and bottom panels. It is evident that the X-ray and radio profiles are different for a part of the halo emission. Radio profiles follow a convex curve while the X-ray is concave in the inner regions (<450 kpc radii). After this, both the radio and the X-ray surface brightness drops rapidly to 800 kpc. The 144 MHz radio and X-ray profiles follow more or less the same trend from 450 kpc to 800 kpc. However, the 675 MHz profile appears flatter than the X-ray profile. In Fig. 13 bottom panel, we show the radial profile of the dimensionless ratio (η)

$$\eta = \frac{I_R}{I_X}, \quad (5)$$

between radio and X-ray surface brightness.

The halo in Abell 2256 does not show a uniform profile of η , see Fig. 13 bottom panel. Both the GMRT and LOFAR profiles first show a decline up to a radius 226 kpc followed by a sharp increase from 226 to 452 kpc. The outermost regions (>452 kpc) show a peculiar trend. It is worth highlighting that within 452 kpc radii, two cold fronts are detected, shown with shaded areas in Fig. 13. The shaded region is wider for CF2 because it extends over various radii. We note that the η profile changes exactly at the location of the cold front CF2, also slightly at CF3, which implies a possible connection. The X-ray discontinuities may have an effect on the spectral and radio versus X-ray profiles. For the halo in Abell 2319, which shows both the halo and the mini-halo characteristic, a similar pattern was reported by Keshet & Loeb (2010): the profile first decreases in the innermost regions and then shows increasing trends.

In Figs. 14 and 15, we show the radio and X-ray profiles extracted separately at the cold fronts CF3 and CF2. The sectors used for extracting these profiles are shown in Fig. 12. For the innermost cold front CF3, there is a jump in both radio (middle) and X-ray (bottom) surface brightness: both decreases at the cold front. A jump is also visible in the spectral index profile (top panel); the spectrum becomes flatter at the cold front.

Similarly, CF2 also shows a small jump in the radio surface brightness profile, see Fig. 15. In contrast to CF3, here the radio and X-ray profiles are quite different for radius <150 kpc; characterized by convex (radio) and concave (X-ray) shapes. At the cold front CF2, the X-ray brightness decreases, whereas the

radio brightness increases. Unlike CF3, the spectral index profile for CF2 does not show a clear jump.

5.6.1. Origin of the core

The core has a steep spectral index and its radio versus X-ray brightness correlation is superlinear. Furthermore, it is confined by the innermost cold front (CF3). A sublinear slope in the radio versus X-ray relation is expected for mini halos (relaxed clusters) produced by sloshing motions (Ignesti et al. 2020).

Origins for the radio halo core could be related to an old radio plasma from previous AGN activity (similar to mini halos) is advected, compressed, and reaccelerated by the activity of the cold front CF3. Simulations indeed suggest that CRE and magnetic field from former activity, confined by cold fronts, can be mixed and advected to the ICM (ZuHone et al. 2021). In this case, it is difficult for CRE to travel from the inside across the cold front to the outside because the magnetic field is probably stirred and aligned along the cold front (ZuHone et al. 2013). We note that ultra-low frequency radio observations show that the spectral index flattens in the core below 43 MHz (Osinga et al., in prep.). The flattening at frequency below 43 MHz seems consistent with the fact that an old plasma mixed and reaccelerated in a relatively small volume (quasi-homogeneous conditions). Another possibility is that the turbulence is less strong in the core with respect to the surrounding region, and the magnetic field is significantly higher than $B_{\text{cmb}}/\sqrt{3}$. Under these conditions, the radio emissivity could be high but the radio spectrum is steep.

5.6.2. Emission outside the halo core

The radio versus X-ray correlation slope steepens when moving from region1 to region2, followed by a flatter slope in region3 while the spectral index steepens radially from region1 to region3. The cold front CF2 lies within region2. Furthermore, the southern shock front falls within region3, where the correlation is almost negligible, as expected in the cluster outskirts for radio relics. However, we have not detected any spectral index gradient associated with the southern shock front.

The change in the correlation slopes and spectral indices from region1- region3 could be due to: (1) Radial decline of

magnetic field : as soon as $B \leq B_{\text{cmb}}/\sqrt{3}$, the radio radial profile becomes steeper, not necessarily superlinear with X-rays (Fig. 13); (2) Increase in the number density of seed particles with radius: less effective Coulomb losses (lower thermal density) and the accumulation of light plasma that is buoyantly transported to the outskirts may increase the number density of available seed electrons and consequently increase the radio emissivity. This results in flattening of the radio versus X-ray relations. Therefore, the flattening of the radio vs. X-ray correlation slopes from region2 to region3 (Fig. 10) could be due to an increase in the number density of seed particles. We emphasize that this does not necessarily produce a flattening in the integrated radio spectrum (Fig. 5) as well; (3) More turbulence in the external regions: this results in decrease in τ_{acc} , that is increases efficiency. As a result, the radio emissivity will increase and the radio spectrum will flatten (for a fixed magnetic field value). This flattening may be balanced by a decline of magnetic field. Since, we do not detect any spectral flattening from region1 to region3, this possibly suggests more magnetic field radial decline).

5.7. Wedge arc

In our total power images (Fig. 2), the wedge arc appears to connect the large relic, the halo and source F. The integrated spectral index of the wedge arc between 144 MHz and 1.5 GHz is $\alpha = -1.63 \pm 0.05$ (see Fig. 5). This value is very similar to the spectral index of the halo region.

The arc is near the outer edge of the detected *Chandra* X-ray emission. However, no X-ray discontinuity was reported at that location. Radio relics generally show a clear spectral index gradient toward the cluster center, a flat spectral index, and a high degree of polarization (Rajpurohit et al. 2020b, 2022b; Loi et al. 2020; Di Gennaro et al. 2022). We do not find any spectral index gradient in this region. Polarized emission is not detected in the wedge arc region (Owen et al. 2014). Furthermore, compared to the larger relic ($\alpha = -1.07$), the arc shows a much steeper spectral index, similar to that of the halo. This, at least rules, out the relic interpretation. It cannot be a radio phoenix, possibly originating from source F because no curvature is found in the overall spectrum. In the radio spectral index versus X-ray surface brightness correlation, the data points from this region show a trend very similar to that found in the radio halo.

One possibility of explaining the wedge arc is that the relativistic plasma from the halo is advected by a complex patterns of fluid motions (vortex-like) that is generated in the tail of the shock of the radio relic. If the spatial diffusion of particles and magnetic field is not fast, relativistic particles and magnetic field are attached to the thermal plasma and basically follow the velocity flow of the gas. The passage of a subcluster (and shock) may thus generate eddies or a vortex at the boundaries downstream that may “shape” the boundary of the halo similar to an arc-shaped wedge structure. In conclusion, on the basis of similar spectral indices and similar trends in the correlation of radio spectral index versus X-ray surface brightness, the radio emission in the wedge arc is most likely associated with the halo, which could be seen in projection with the relic and source F.

5.8. Source AI

Source AI is located in the outskirts of the cluster and shows an ultra-steep spectral index, about -1.9 between 350 and 675 MHz. The source is not detected at 1–2 GHz and the integrated spectral index between 144 MHz and 675 MHz is already

curved. Optical images do not reveal any obvious counterpart (van Weeren et al. 2009a). The source could be a AGN remnant or radio phoenix. AGN remnants originate from a previous episode that left a fossil population from a nearby AGN. On the other hand, radio phoenixes are produced by adiabatic compression of AGN fossil radio plasma by the passage of a shock front in the ICM (Ensslin et al. 1998).

In the high resolution radio images, we cannot identify any related radio galaxy associated with AI. On the basis of the morphology, location, total extent, steep spectral index, and curved integrated spectrum, we classify the source as a radio phoenix.

6. Summary and conclusions

In this work, we have presented a new detailed analysis of the radio halo in the famous galaxy cluster Abell 2256. Previous studies of the halo have been limited by their low resolution and sparser *uv*-coverage. Our deep , high fidelity observations, in combination with the available X-ray observations, provide crucial insights into the origin of the radio halo. We summarize our main findings as follows:

1. We show the first deep, high spatial resolution (12–20′) radio images of the central halo. The halo emission is detected at all frequencies, namely 144 MHz, 350 MHz, 675 MHz and 1.5 GHz. The LLS size of the halo is about 0.9 Mpc at 144 MHz and 0.5 Mpc at 1.5 GHz, implying that the outermost region of the halo has a steep spectrum.
2. Despite the complex ICM distribution, the radio halo morphology is remarkably similar to that in X-ray. In particular, the X-ray peak in the main mass component coincides with the radio peak. Moreover, the radio surface brightness, within the main component, is confined by the innermost cold front.
3. The overall emission from the halo follows a power-law spectrum between 144 MHz and 1.5 GHz, and has an ultra-steep spectrum with an integrated spectral index of -1.63 ± 0.03 . According to turbulent reacceleration models, the absence of any steepening at high frequency in the integrated spectrum suggests that the emitting volume is not homogeneous. At the cluster core (or centroid), we find evidence of an ultra-steep spectral index ($\alpha = -1.60$) while the surrounding region is flatter ($\alpha = -1.45$).
4. The spatially resolved spectral index maps reveal a spectral steepening with increasing radius. We find small-scale fluctuations in the spectral index across the halo, on scales of about 20 kpc.
5. The halo fits well with the known radio power-mass correlation of other halos at 144 MHz. However, it is significantly underluminous with respect to the radio power-mass correlation at 1.4 GHz. This is in line with current models where ultra-steep spectrum are generally underluminous.
6. The point-to-point comparison between the radio and X-ray surface brightness across the halo reveals a strong sublinear correlation. The correlation slope flattens at higher frequencies. There are substructures: the halo core shows a super-linear slope ($I_R \propto I_X^{1.51}$) while the outermost fainter region shows a sublinear slope ($I_R \propto I_X^{0.41}$). We suggest the core emission is related to old plasma from previous AGN activity, being advected, compressed and reaccelerated by the nearby cold front. Another possibility is that the turbulence is less strong in the core and magnetic field is high making the spectrum steep. The change in the radio vs. X-ray correlation

slope in the other region2 and region3 could be due to magnetic field radial decline, increasing number density of seed particles or more turbulence in the outermost regions.

7. We find a strong anticorrelation between the spectral index and the X-ray surface brightness across the halo. This is consistent with radial steepening, the outermost steeper part corresponds to regions with less dense ICM, that is less turbulence and a decline in the magnetic fields.
8. The radio spectral index versus X-ray correlation across the arc-shaped wedge structure to the east of the cluster center, connecting the source F to the relic and the halo, show trends similar to that of the halo. The integrated spectrum of this structure is also very similar to the halo, hinting that the radio emission in the wedge arc is likely a part of the halo.
9. A diffuse elongated source to the southeast (source AI) fits the profile of a radio “phoenix” produced by adiabatic compression of fossil radio plasma due to a merger shock front.

To summarize, our new results stress once more that the radio halo in Abell 2256 is a very peculiar object, whose study can lead to new progress in our understanding of particle acceleration mechanisms on very large scales. First, a number of observed features are in line with turbulent reacceleration models for the origin of radio emitting electrons. For example, its ultra-steep integrated spectrum, the different spectral indices in the subregions, the spectral steepening with increasing radius, the spectral index fluctuations, the sublinear radio versus X-ray correlation slope and the fact that it is underluminous at high frequency. On the other hand, not all the observable evidence can be explained by turbulent acceleration models, requiring for updates on the model (e.g., the ultra-steep spectral index and the superlinear radio versus X-ray correlation slope in the core region, the connection of the radio emission with the cold fronts, and the radio versus X-ray correlation trends in the halo subregions). Our results suggest that none of the proposed models for halo formation can explain all the observational findings at the same time.

In conclusion, the emerging complexity in the radio halo properties that we are able to observe with the new generation radio telescopes is providing clear evidence that homogeneous models are too simple to explain all the observed features in this class of sources. For example, the Coma (Bonafede et al. 2022) and Abell 2256 halos are among the closest clusters, and we already started seeing differences between them. Our results highlight the need for additional theoretical work, with more detailed and specific predictions, on particle acceleration in radio halos.

Acknowledgements. KR and FV acknowledge financial support from the ERC Starting Grant “MAGCOW” no. 714196. RJvW acknowledges support from the ERC Starting Grant ClusterWeb 804208. AB acknowledges support from the VIDJ research programme with project number 639.042.729, which is financed by the Netherlands Organisation for Scientific Research (NWO). A. Botteon, A. Bonafede, CJR, EB, and CS acknowledges support from the ERC through the grant ERC-Stg DRANOEL n. 714245. W.F. acknowledges support from the Smithsonian Institution and the *Chandra* High Resolution Camera Project through NASA contract NAS8-03060. AD acknowledges support by the BMBF Verbundforschung under the grant 05A20STA. MB acknowledges support from the Deutsche Forschungsgemeinschaft under Germany’s Excellence Strategy-EXC 2121 “Quantum Universe” -390833306. MR acknowledges support from INAF mainstream project “Galaxy Clusters science with LOFAR”. The GMRT is run by the National Centre for Radio Astrophysics (NCRA) of the Tata Institute of Fundamental Research (TIFR). LOFAR (van Haarlem et al. 2013) is the Low Frequency Array designed and constructed by ASTRON. It has observing, data processing, and data storage facilities in several countries, which are owned by various parties (each with their own funding sources), and that are collectively operated by the ILT foundation under a joint scientific policy. The ILT resources have benefited from the following recent major funding sources: CNRS-INSU, Observatoire de Paris and Université d’Orléans, France; BMBF, MIWF-NRW,

MPG, Germany; Science Foundation Ireland (SFI), Department of Business, Enterprise and Innovation (DBEI), Ireland; NWO, The Netherlands; The Science and Technology Facilities Council, UK; Ministry of Science and Higher Education, Poland; The Istituto Nazionale di Astrofisica (INAF), Italy. This research made use of the LOFAR-UK computing facility located at the University of Hertfordshire and supported by STFC [ST/P000096/1], and of the LOFAR-IT computing infrastructure supported and operated by INAF, and by the Physics Dept. of Turin University (under the agreement with Consorzio Interuniversitario per la Fisica Spaziale) at the C3S Supercomputing Centre, Italy.

References

- Ackermann, M., Ajello, M., Albert, A., et al. 2014, *ApJ*, 787, 18
 Ackermann, M., Ajello, M., Albert, A., et al. 2016, *ApJ*, 819, 149
 Adam, R., Goksu, H., Brown, S., Rudnick, L., & Ferrari, C. 2021, *A&A*, 648, A60
 Beresnyak, A., Xu, H., Li, H., & Schlickeiser, R. 2013, *ApJ*, 771, 131
 Berrington, R. C., Lugger, P. M., & Cohn, H. N. 2002, *AJ*, 123, 2261
 Biava, N., de Gasperin, F., Bonafede, A., et al. 2021, *MNRAS*, 508, 3995
 Bonafede, A., Brunetti, G., Rudnick, L., et al. 2022, *ApJ*, 933, 218
 Botteon, A., Brunetti, G., Ryu, D., & Roh, S. 2020a, *A&A*, 634, A64
 Botteon, A., Brunetti, G., van Weeren, R. J., et al. 2020b, *ApJ*, 897, 93
 Bourdin, H., & Mazzotta, P. 2008, *A&A*, 479, 307
 Boxelaar, J. M., van Weeren, R. J., & Botteon, A. 2021, *Astron. Comput.*, 35, 100464
 Brentjens, M. A. 2008, *A&A*, 489, 69
 Breuer, J. P., Werner, N., Mernier, F., et al. 2020, *MNRAS*, 495, 5014
 Bridle, A. H., & Fomalont, E. B. 1976, *A&A*, 52, 107
 Bridle, A. H., Fomalont, E. B., Miley, G. K., & Valentijn, E. A. 1979, *A&A*, 80, 201
 Briel, U. G., & Henry, J. P. 1994, *Nature*, 372, 439
 Briel, U. G., Henry, J. P., Schwarz, R. A., et al. 1991, *A&A*, 246, L10
 Brunetti, G., & Jones, T. W. 2014, *Int. J. Mod. Phys. D*, 23, 1430007
 Brunetti, G., & Lazarian, A. 2007, *MNRAS*, 378, 245
 Brunetti, G., & Lazarian, A. 2016, *MNRAS*, 458, 2584
 Brunetti, G., Setti, G., Feretti, L., & Giovannini, G. 2001, *MNRAS*, 320, 365
 Brunetti, G., Giacintucci, S., Cassano, R., et al. 2008, *Nature*, 455, 944
 Brunetti, G., Blasi, P., Reimer, O., et al. 2012, *MNRAS*, 426, 956
 Brunetti, G., Zimmer, S., & Zandanel, F. 2017, *MNRAS*, 472, 1506
 Bruno, L., Rajpurohit, K., Brunetti, G., et al. 2021, *A&A*, 650, A44
 Cassano, R. 2010, *A&A*, 517, A10
 Cassano, R., & Brunetti, G. 2005, *MNRAS*, 357, 1313
 Cassano, R., Brunetti, G., & Setti, G. 2006, *MNRAS*, 369, 1577
 Cassano, R., Etori, S., Giacintucci, S., et al. 2010, *ApJ*, 721, L82
 Cassano, R., Etori, S., Brunetti, G., et al. 2013, *ApJ*, 777, 141
 Chandra, P., Ray, A., & Bhatnagar, S. 2004, *ApJ*, 612, 974
 Clarke, T. E., & Ensslin, T. A. 2006, *AJ*, 131, 2900
 Cova, F., Gastaldello, F., Wik, D. R., et al. 2019, *A&A*, 628, A83
 Cuciti, V., Brunetti, G., van Weeren, R., et al. 2018, *A&A*, 609, A61
 Cuciti, V., Cassano, R., Brunetti, G., et al. 2021, *A&A*, 647, A51
 Dallacasa, D., Brunetti, G., Giacintucci, S., et al. 2009, *ApJ*, 699, 1288
 de Gasperin, F., Rudnick, L., Finoguenov, A., et al. 2022, *A&A*, 659, A146
 Di Gennaro, G., van Weeren, R. J., Hoeft, M., et al. 2018, *ApJ*, 865, 24
 Di Gennaro, G., van Weeren, R. J., Brunetti, G., et al. 2021, *Nat. Astron.*, 5, 268
 Di Gennaro, G., van Weeren, R. J., Rudnick, L., et al. 2022, *ApJ*, 911, 3
 Donnert, J., Dolag, K., Brunetti, G., & Cassano, R. 2013, *MNRAS*, 429, 3564
 Duchesne, S. W., Johnston-Hollitt, M., & Wilber, A. G. 2021, *PASA*, 38, e031
 Ebeling, H., Edge, A. C., Bohringer, H., et al. 1998, *MNRAS*, 301, 881
 Ensslin, T. A., Biermann, P. L., Klein, U., & Kohle, S. 1998, *A&A*, 332, 395
 Fabricant, D. G., Kent, S. M., & Kurtz, M. J. 1989, *ApJ*, 336, 77
 Fanaroff, B. L., & Riley, J. M. 1974, *MNRAS*, 167, 31P
 Ge, C., Liu, R.-Y., Sun, M., et al. 2020, *MNRAS*, 497, 4704
 Giovannini, G., & Feretti, L. 2000, *New A*, 5, 335
 Govoni, F., Enßlin, T. A., Feretti, L., & Giovannini, G. 2001a, *A&A*, 369, 441
 Govoni, F., Feretti, L., Giovannini, G., et al. 2001b, *A&A*, 376, 803
 Hoang, D. N., Shimwell, T. W., Stroe, A., et al. 2017, *MNRAS*, 471, 1107
 Hoang, D. N., Shimwell, T. W., van Weeren, R. J., et al. 2019, *A&A*, 622, A20
 Hoang, D. N., Zhang, X., Stuardi, C., et al. 2021, *A&A*, 656, A154
 Hoeft, M., Dumba, C., Drabant, A., et al. 2021, *A&A*, 654, A68
 Ignesti, A., Brunetti, G., Gitti, M., & Giacintucci, S. 2020, *A&A*, 640, A37
 Intema, H. T., van der Tol, S., Cotton, W. D., et al. 2009, *A&A*, 501, 1185
 Kale, R., & Dwarakanath, K. S. 2010, *ApJ*, 718, 939
 Kelly, B. C. 2007, *ApJ*, 665, 1489
 Keshet, U., & Loeb, A. 2010, *ApJ*, 722, 737
 Kim, K. T. 1999, *J. Korean Astron. Soc.*, 32, 75
 Loi, F., Murgia, M., Vacca, V., et al. 2020, *MNRAS*, 498, 128
 Macario, G., Markevitch, M., Giacintucci, S., et al. 2011, *ApJ*, 728, 82

- Markevitch, M., & Vikhlinin, A. 1997, *ApJ*, 491, 467
- Markevitch, M., Govoni, F., Brunetti, G., & Jerius, D. 2005, *ApJ*, 627, 733
- Miller, N. A., Owen, F. N., & Hill, J. M. 2003, *AJ*, 125, 2393
- Miniati, F. 2015, *ApJ*, 800, 60
- Molendi, S., De Grandi, S., & Fusco-Femiano, R. 2000, *ApJ*, 534, L43
- Murgia, M., Govoni, F., Markevitch, M., et al. 2009, *A&A*, 499, 679
- Offringa, A. R., McKinley, B., Hurley-Walker, N., et al. 2014, *MNRAS*, 444, 606
- Orrú, E., Murgia, M., Feretti, L., et al. 2007, *A&A*, 467, 943
- Owen, F. N., Rudnick, L., Eilek, J., et al. 2014, *ApJ*, 794, 24
- Pearce, C. J. J., van Weeren, R. J., Andrade-Santos, F., et al. 2017, *ApJ*, 845, 81
- Perley, R. A., & Butler, B. J. 2013, *ApJS*, 204, 19
- Petrosian, V. 2001, *ApJ*, 557, 560
- Pinzke, A., Oh, S. P., & Pfrommer, C. 2017, *MNRAS*, 465, 4800
- Planck Collaboration XI. 2011, *A&A*, 536, A11
- Rajpurohit, K., Hoeft, M., van Weeren, R. J., et al. 2018, *ApJ*, 852, 65
- Rajpurohit, K., Hoeft, M., Vazza, F., et al. 2020a, *A&A*, 636, A30
- Rajpurohit, K., Vazza, F., Hoeft, M., et al. 2020b, *A&A*, 642, L13
- Rajpurohit, K., Brunetti, G., Bonafede, A., et al. 2021a, *A&A*, 646, A135
- Rajpurohit, K., Vazza, F., van Weeren, R. J., et al. 2021b, *A&A*, 654, A41
- Rajpurohit, K., van Weeren, R. J., Hoeft, M., et al. 2022a, *ApJ*, 927, 80
- Rajpurohit, K., Hoeft, M., Wittor, D., et al. 2022b, *A&A*, 657, A2
- Riseley, C. J., Rajpurohit, K., Loi, F., et al. 2022a, *MNRAS*, 512, 4210
- Riseley, C. J., Bonnassieux, E., Vernstrom, T., et al. 2022b, *MNRAS*, 515, 1871
- Roettiger, K., Burns, J. O., & Pinkney, J. 1995, *ApJ*, 453, 634
- Rottgering, H., Snellen, I., Miley, G., et al. 1994, *ApJ*, 436, 654
- Shimwell, T. W., Brown, S., Feain, I. J., et al. 2014, *MNRAS*, 440, 2901
- Shimwell, T. W., Hardcastle, M. J., Tasse, C., et al. 2022, *A&A*, 659, A1
- Sun, M., Murray, S. S., Markevitch, M., & Vikhlinin, A. 2002, *ApJ*, 565, 867
- Tasse, C., Shimwell, T., Hardcastle, M. J., et al. 2021, *A&A*, 648, A1
- Trasatti, M., Akamatsu, H., Lovisari, L., et al. 2015, *A&A*, 575, A45
- Vacca, V., Govoni, F., Murgia, M., et al. 2011, *A&A*, 535, A82
- Vacca, V., Feretti, L., Giovannini, G., et al. 2014, *A&A*, 561, A52
- van Haarlem, M. P., Wise, M. W., Gunst, A. W., et al. 2013, *A&A*, 556, A2
- van Weeren, R. J., Röttgering, H. J. A., Brügger, M., & Cohen, A. 2009a, *A&A*, 505, 991
- van Weeren, R. J., Intema, H. T., Oonk, J. B. R., Röttgering, H. J. A., & Clarke, T. E. 2009b, *A&A*, 508, 1269
- van Weeren, R. J., Röttgering, H. J. A., Brügger, M., & Hoeft, M. 2010, *Science*, 330, 347
- van Weeren, R. J., Röttgering, H. J. A., Rafferty, D. A., et al. 2012, *A&A*, 543, A43
- van Weeren, R. J., Brunetti, G., Brügger, M., et al. 2016, *ApJ*, 818, 204
- van Weeren, R. J., Ogrean, G. A., Jones, C., et al. 2017, *ApJ*, 835, 197
- van Weeren, R. J., de Gasperin, F., Akamatsu, H., et al. 2019, *Space Sci. Rev.*, 215, 16
- van Weeren, R. J., Shimwell, T. W., Botteon, A., et al. 2021, *A&A*, 651, A115
- Wilber, A., Brügger, M., Bonafede, A., et al. 2018, *MNRAS*, 473, 3536
- Xie, C., van Weeren, R. J., Lovisari, L., et al. 2020, *A&A*, 636, A3
- ZuHone, J. A., Markevitch, M., Brunetti, G., & Giacintucci, S. 2013, *ApJ*, 762, 78
- ZuHone, J. A., Markevitch, M., Weinberger, R., Nulsen, P., & Ehlert, K. 2021, *ApJ*, 914, 73